

REPORT DOCUMENTATION PAGE			Form Approved OMB No. 0704-0188		
Public reporting burden for this collection of information is estimated to average 1 hour per response, including the time for reviewing instructions, searching existing data sources, gathering and maintaining the data needed, and completing and reviewing this collection of information. Send comments regarding this burden estimate or any other aspect of this collection of information, including suggestions for reducing this burden to Department of Defense, Washington Headquarters Services, Directorate for Information Operations and Reports (0704-0188), 1215 Jefferson Davis Highway, Suite 1204, Arlington, VA 22202-4302. Respondents should be aware that notwithstanding any other provision of law, no person shall be subject to any penalty for failing to comply with a collection of information if it does not display a currently valid OMB control number. PLEASE DO NOT RETURN YOUR FORM TO THE ABOVE ADDRESS.					
1. REPORT DATE (DD-MM-YYYY) 07-25-2017		2. REPORT TYPE Final		3. DATES COVERED (From - To) 01/02/2013 to 30/04/2017	
4. TITLE AND SUBTITLE Slotted Waveguide and Antenna Study for HPM & RF Applications		5a. CONTRACT NUMBER N00014-13-1-0415			
		5b. GRANT NUMBER N00014-13-1-0415			
		5c. PROGRAM ELEMENT NUMBER			
6. AUTHOR(S) Christos Christodoulou		5d. PROJECT NUMBER			
		5e. TASK NUMBER			
		5f. WORK UNIT NUMBER			
7. PERFORMING ORGANIZATION NAME(S) AND ADDRESS(ES) University of New Mexico		8. PERFORMING ORGANIZATION REPORT NUMBER			
9. SPONSORING / MONITORING AGENCY NAME(S) AND ADDRESS(ES) AFRL		10. SPONSOR/MONITOR'S ACRONYM(S)			
		11. SPONSOR/MONITOR'S REPORT NUMBER(S)			
12. DISTRIBUTION / AVAILABILITY STATEMENT Public					
13. SUPPLEMENTARY NOTES					
14. ABSTRACT An S-band longitudinal slotted waveguide antenna was designed to perform as a uniform array. The antenna was investigated for its power handling capability. The input power threshold for both air breakdown and multipaction were studied. The radiation pattern measured in high power testing with a magnetron providing 500 ns long and 0.8 MW peak pulses, demonstrated good agreement with the simulated radiation pattern. This source power level was below the predicted maximum input power handling capability of 1.8 MW, at high elevation (in Albuquerque, NM). No breakdown was observed during the experiment. To further reduce the size of the antenna array, a narrow-band, rugged, complementary-split-ring (CSR) slotted waveguide antenna (SWA) was designed and fabricated. Both simulation and experimental results showed that the complementary-split-ring slot radiates a linearly polarized wave with high efficiency. The CSR slotted waveguide antenna provided, approximately, 55% size reduction, compared to currently available SWA designs, with high directivity, low return loss, and very high power handling capability for S-band applications Finally, a new approach to prototyping CSR-SWA antennas for high-power microwave applications by using 3D printing					
15. SUBJECT TERMS Slotted waveguide arrays, High power microwaves, 3D printed antennas, multipaction, complementary-split-ring waveguide arra					
16. SECURITY CLASSIFICATION OF:			17. LIMITATION OF ABSTRACT	18. NUMBER OF PAGES	19a. NAME OF RESPONSIBLE PERSON
a. REPORT	b. ABSTRACT	c. THIS PAGE			19b. TELEPHONE NUMBER (include area code)



THE UNIVERSITY of
NEW MEXICO

SCHOOL of ENGINEERING

Department of Electrical & Computer Engineering

“Slotted Waveguide and Antenna Study for HPM & RF Applications”

Final Technical Report

ONR Grant #: N00014-13-1-0415

01 February 2013 – 30 April 2017

July 25 2017

Submitted by:

Christos Christodoulou— Principal Investigator
Department of Electrical and Computer Engineering
University of New Mexico
Albuquerque, NM 87131
Tel. (505) 277-6580
e-mail: christos@unm.edu

This material is based on research sponsored by the Office of Naval Research under agreement number N00014-13-1-0415. The U.S. Government is authorized to reproduce and distribute reprints for Governmental purposes notwithstanding any copyright notation thereon.

Distribution Statement A: Approved for public release; distribution unlimited

TABLE OF CONTENTS

LIST OF ACRONYMS	3
LIST OF FIGURES.....	4
I. SUMMARY OF ACHIEVEMENTS	6
II. INTRODUCTION	7
III. DETAILED RESULTS OF THE PROJECT	10
1. Narrow-wall longitudinal slotted waveguide antenna design for HPM applications	10
1.1 S-band narrow-wall longitudinal-slot array waveguide antenna.....	10
1.2 Collaboration with NSWC Dahlgren.....	13
1.3 Collaboration with Air Force Research Laboratory	15
1.4 Power handling capability estimation for slotted waveguide antennas.....	18
Power handling capability estimation determined by air break down (outside the antenna).....	18
Power handling capability estimation determined by multipaction (inside the antenna).....	20
2. Miniaturization of narrow-wall slotted waveguide antenna designs.....	23
2.1 Periodic structures applied for antenna miniaturization and beam-steering..	23
Split-ring-loaded waveguide:.....	23
Double narrow-wall longitudinal-slot array waveguide antenna:	25
2.2 A Compact S-band narrow-wall complementary-split-ring slotted waveguide antenna	27
Complementary-split-ring slots in the narrow-wall of a rectangular waveguide	27
Microwave network analysis	30
Narrow-wall complementary-split-ring slotted waveguide antenna	34
Complementary-split-ring slotted waveguide antenna loaded with periodic air-filled corrugations	37
Complementary-split-ring slotted waveguide antenna array	39
3. 3D printed HPM antennas.....	43
3D printed HPM antennas on ABS.....	43
3D printed HPM antennas on Bluestone (SLA printing).....	46
IV. CONCLUSIONS	49
V. List of publications	51
APPENDIX I	52
Slotted circular cylinder resonators.....	52

<h2 style="text-align: center;">LIST OF ACRONYMS</h2>

<u>Acronym</u>	<u>Definition</u>
ABS	Acrylonitrile Butadiene Styrene
APS	Antennas and Propagation Society
CRLH	Composite Right/left-Handed
CSR	Complementary Split Ring
CST	Computer Simulation Technology
ECCS	European Cooperation for Space Standardization
EMI	Electromagnetic Frequency Interference
HPB	H-plane Bend
HPM	High Power Microwave
HFSS	High Frequency Structure Simulator
IEEE	Institute of Electrical and Electronics Engineers
RF	Radio Frequency
RFI	Radio Frequency Interference
SCCR	Slotted Circular Cylinder Resonator
SLA	Stereo lithography
SRR	Split Ring Resonator
SWA	Slotted Waveguide Antenna
URSI	International Union of Radio Science
USNC	United States National Committee

LIST OF FIGURES

Figure 1 S-band & X-band narrow-wall longitudinal slot array waveguide antenna..	10
Figure 2 Simulated and measured S parameter	10
Figure 3 Radiation Pattern Set-up.....	11
Figure 4 Normalized radiation pattern of narrow-wall longitudinal-slot array waveguide antenna: a) H-plane, b) E-plane.	11
Figure 5 Schematic and H-plane radiation pattern of double-array design.....	12
Figure 6 Schematic and axial ratio of circularly-polarized-array design.....	13
Figure 7 Measured return loss of the S-band narrow-wall longitudinal-slot array waveguide antenna.....	14
Figure 8 Simulated and measured H-plane radiation pattern of the S-band narrow-wall longitudinal-slot array waveguide antenna.....	14
Figure 9 Simulated and measured E-plane radiation pattern of the S-band narrow-wall longitudinal-slot array waveguide antenna.....	15
Figure 10 Block diagram of hot test setup	15
Figure 11 High power microwave source: S-Band Magnetron	16
Figure 12 Radiation pattern measurement setup inside anechoic chamber.....	16
Figure 13 Diagram of H-plane radiation pattern measurements	17
Figure 14 Antenna gain within the main-beam	18
Figure 15 E field distribution simulated by HFSS.....	19
Figure 16 Power threshold estimation by CST.....	21
Figure 17 Number of electrons inside the antenna for input power of 2.35MW, 2.54MW and 2.75MW	22
Figure 18 Distribution of the electrons inside the antenna ($P_{in}=2.35MW$)	23
Figure 19 Distribution of the electrons inside the antenna ($P_{in}=2.54MW$)	23
Figure 20 Schematic of HPB-radiator loaded with an SRR-array (overlapping placement of rings).....	24
Figure 21 S11 of H-plane-bend radiator loaded with an SRR-array.....	24
Figure 22 3D radiation pattern & E-field polarization of HPB-radiator loaded with an SRR array	25
Figure 23 Schematic of double narrow-wall longitudinal-slot array waveguide antenna and its 3D radiation pattern	26
Figure 24 Configuration of CRLH waveguide structure.....	26
Figure 25 Azimuth plane radiation pattern for different lengths of short stubs of left-handed/right-handed waveguide.....	27
Figure 26 Design parameters of the CSR slot	28
Figure 27 S11 vs R	29
Figure 28 S11 vs α	29
Figure 29 S11 vs w.....	30
Figure 30 Equivalent microwave network of the slot array	32
Figure 31 Comparison of the CSR-SWA with the longitudinal slot array (same inter-element spacing).....	34

Figure 32 schematic of the CSR-SWA.....	35
Figure 33 aluminum plates fabricated by Waterjet Cutting.....	35
Figure 34 Simulated and measured S11 of the CSR-SWA.....	36
Figure 35 Comparison of the CSR-SWA and the longitudinal SWA.....	36
Figure 36 Radiation pattern measurement set-up for the CSR-SWA	37
Figure 37 Measured & simulated normalized radiation pattern of the CSR-SWA.....	37
Figure 38 Periodic corrugations added to the other narrow-wall of the CSR-SWA....	38
Figure 39 H plane radiation pattern of the CSR-SWA and the CSR-SWA loaded with corrugations	39
Figure 40 E plane radiation pattern of the CSR-SWA and the CSR-SWA loaded with corrugations	39
Figure 41 Schematic of the CSR-SWA double array	40
Figure 42 E-plane radiation pattern of the CSR-SWA double array and the longitudinal slotted waveguide antenna.....	41
Figure 43 H-plane radiation pattern of the CSR-SWA double array and the longitudinal slotted waveguide antenna.....	41
Figure 44 Normalized E-plane radiation pattern of the CSR-SWA double array and the single CSR-SWA.....	42
Figure 45 Normalized H-plane radiation pattern of the CSR-SWA double array and the single CSR-SWA.....	42
Figure 46 3D printed CSR-SWA and aluminum CSR-SWA (on the right). Antenna one the left is the metallic version.....	43
Figure 47 A 3D printed CSR-SWA applied with MG chemical 843 conductive coating	44
Figure 48 Schematic of 3D printed CSR-SWA with conductive coatings	45
Figure 49 S11 values of 3D printed CSR-SWA with MG chemical 843	45
Figure 50 H-plane radiation pattern of 3D printed modified CSR-SWA with conductive coating	46
Figure 51 E-plane radiation pattern of 3D printed modified CSR-SWA with conductive coating	46
Figure 52 SLA printed CSR-SWA plated with copper.....	47
Figure 53 Geometry of SCCR structure with nonzero thickness	53

I. SUMMARY OF ACHIEVEMENTS

This technical report presents the work performed during the time span of 2013-2017 of ONR N00014-13-1-0415 contract. The achievements can be listed as follows:

a) Narrow-wall longitudinal slotted waveguide antenna design for HPM applications

- i) A high-gain, S band narrow-wall, longitudinal-slot array waveguide antenna design was proposed. The proposed antenna model was fabricated and tested at the University of New Mexico. Further research on a double array design, a curved antenna design, and a circularly polarized antenna design was performed through HFSS simulations.
- ii) The University of New Mexico has collaborated with NSWC Dahlgren on fabricating and testing an S-band, narrow-wall, longitudinal-slot array waveguide antenna. Its high power handling capability has been tested.
- iii) The University of New Mexico has also collaborated with the Air Force Research Laboratory in Albuquerque, NM on testing the high power capabilities of the S-band narrow-wall longitudinal-slot array waveguide antenna. A paper was submitted to the APS/URSI 2017 reporting the experiments performed both at the University of New Mexico and at the Air Force Research Laboratory in Albuquerque.
- iv) The power handling capability estimation for slotted waveguide antenna was performed, through ANSYS HFSS and CST Particle-in-cell solver. A paper was submitted to the journal of IEEE Antennas and Wireless Propagation Letters.

b) Miniaturization of narrow-wall slotted waveguide antenna designs

- i) A periodic structure using split-ring-resonators was applied to the narrow-wall slotted waveguide antenna for size miniaturization in either transverse cross section or longitudinal length of the waveguide. A paper was submitted to and presented at 2014 USNC-URSI, National Radio

Science meeting. A new double narrow-wall longitudinal-slot array design was proposed to reduce the side-lobe level. A paper was submitted to and presented at the APS/URSI 2014 conference.

- ii) A narrow-wall, **complementary-split-ring slotted** waveguide antenna design was proposed for antenna size reduction. This was the first time that such a slot structure was used as a radiating element in slotted array waveguide antennas. The proposed narrow-wall complementary-split ring slots provide similar radiation characteristics, i.e. efficiency, gain, polarization etc., as the conventional, half-wavelength longitudinal slots, while reducing the slot dimension to 0.229λ . An antenna prototype was fabricated and tested at the University of New Mexico. A paper was submitted to and presented at the APS/URSI 2015. Additionally, a journal paper was submitted to the IEEE Transactions on Antennas and Propagation in 2017.

c) 3D printing technology for fast prototyping of complex, light weigh HPM antenna structures

- i) 3D printing technology has been applied to the fabrication of the narrow-wall complementary-split-ring slotted waveguide antenna design, due to the complexity of its design, and precision required of the fabrication of the CSR-slots. A couple of antenna prototypes were built at UNM and tested. The 3D printed antenna models were either spray painted with conductive paint or electro-plated. A paper was submitted and presented at the APS/URSI 2016.

II. INTRODUCTION

1. High-power microwave antennas

Recently, high power microwave (HPM) structure technology has seen major developments in size reduction as well as increase in efficiency [1]. Electronics have

been proven to be vulnerable to various high power generated waveforms [2-5]. Key devices to develop HPM systems are high power microwave antennas. HPM antennas can provide very intense electric field (E-field) covering a narrow band to ultra-wideband spectrums. Such antennas require a gain as high as possible, side lobes as low as possible, and withstand input power as high as possible. Depending on the application and mainly on the feeding HPM source (magnetrons, backward-wave oscillators (BWO), magnetically insulated line oscillators (MILO), Marx generators, etc.), designs of HPM antennas have been proposed in the form of parabolic antennas [6], slotted waveguide antennas [7], lens antennas [8], reflect array antennas [9], radial transmission helix arrays [10], etc.

In this work, the design of an air-filled slotted rectangular waveguide antenna has been considered for its ruggedness and high-power handling capability. This type of antenna provides high directivity, low return loss as well as mechanical structural strength. The need to miniaturize the antenna size to fit the platform also leads us to the design of slotted waveguide antennas due to their compact structure.

2. Miniaturization of the slotted waveguide antenna designs

This type of half-wavelength slotted waveguide antennas tend to be bulky and heavy due to its all metallic structure. The reduction of the array size without losing its radiation performance is limited by the size of the half-wavelength longitudinal slots. Recently, single split-ring resonators have been placed underneath longitudinal slots to reduce slots size while maintaining a similar gain and efficiency [11-12]. The split-ring resonators must be designed to match the desired resonant frequency, as well as be precisely placed underneath the slot, to increase the field intensity. Thus, the complexity of manufacturing increases significantly. Also, the reduction in size is limited to $0.25\lambda_0$ without a loss of radiation performance.

To further reduce the size of the slot dimensions and to overcome the associated manufacturing complexities, an alternative approach is required. A split-ring slot cut

in the broad-wall of a rectangular waveguide was proposed and investigated [13-14]. The outer diameter of such split ring slot cuts was shown to reduce the individual slot dimensions from $0.5\lambda_0$ to $0.186\lambda_0$, yielding a more compact array antenna with similar radiation characteristics as the conventional half-wavelength slot arrays.

3. 3D printing technology for high-power-microwave applications

Additive manufacturing or 3-D printing is a technology that enables the fabrication of complex objects directly from a digital model. Three-dimensional printing is achieved by laying down successive layers, each of slightly different shape. This technology has been evolving quite rapidly in recent years and is nowadays seen as an alternative to traditional manufacturing methods. Potential applications of 3-D printing have expanded from its origins in the fabrication of mechanical objects to the incorporation of electrical circuits in the manufacturing process [15]. It has the potential to provide a number of benefits to high power microwave (HPM) systems, including weight reduction, rapid prototyping, or the fabrication of extremely complex shapes. An obvious concern is that these benefits may come at the cost of a reduction in performance or durability.

Recently, the performance of two 3D printed anode structures, metallized via electroplating and thermal spraying, in a relativistic planar magnetron was reported in [16]. It was shown that both 3D printed anode structures provide similar microwave performance compared to a machined aluminum anode. Over a limited set of shots, no damage or degradation was observed. A slow wave structure (metamaterial-like) was fabricated using 3D printing in [17]. This structure was tested in the mega watt class and no breakdown, attributable to the surface roughness, introduced by additive manufacturing, was observed in the experiments.

III. DETAILED RESULTS OF THE PROJECT

1. Narrow-wall longitudinal slotted waveguide antenna design for HPM applications

1.1 S-band narrow-wall longitudinal-slot array waveguide antenna

A high-gain, S-band narrow-wall longitudinal-slot array waveguide antenna design for high-power microwave applications was proposed in [18]. The proposed antenna operates at 3.17GHz with a return loss of -32dB. Measurement results show that the antenna provides a fan-beam radiation pattern, as predicted by HFSS simulations. Figure 1 shows the S-band, narrow-wall longitudinal-slot array waveguide antenna model along with the X band antenna model. Figure 2 presents simulated and measured return loss results of the S-band narrow-wall longitudinal-slot array.



Figure 1. S-band & X-band narrow-wall longitudinal slot array waveguide antenna

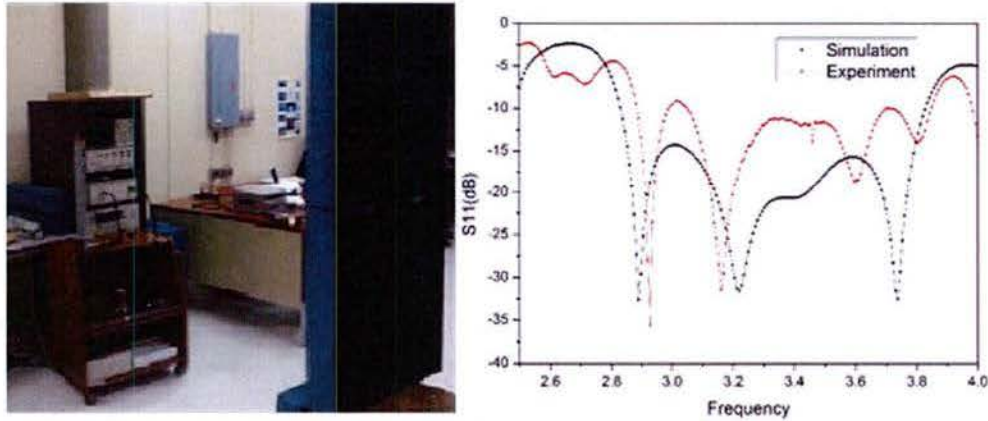


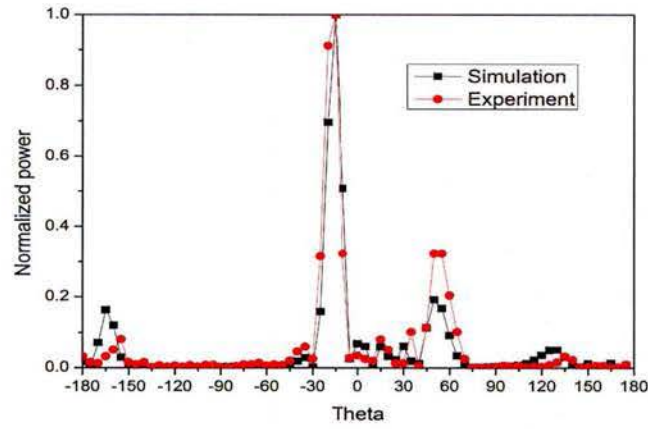
Figure 2. Simulated and measured S parameter

Figure 3 shows the radiation pattern measurement set-up and Figure 4 depicts the

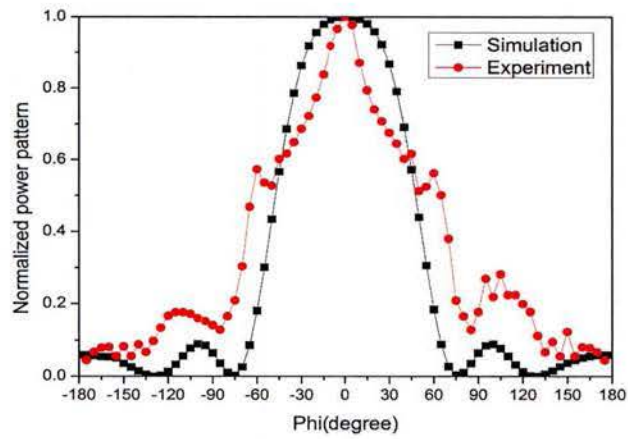
simulated and measured radiation pattern of the S-band narrow-wall longitudinal-slot array design. Table 1 shows predictions of the power handling capability for the S-band narrow-wall longitudinal-slot array design in different air pressure cases.



Figure 3. Radiation Pattern Set-up



a) H-plane



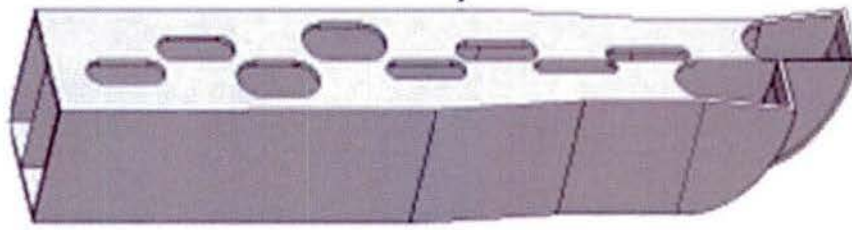
b) E-plane

Figure 4. Normalized radiation pattern of narrow-wall longitudinal-slot array waveguide antenna: a) H-plane, b) E-plane.

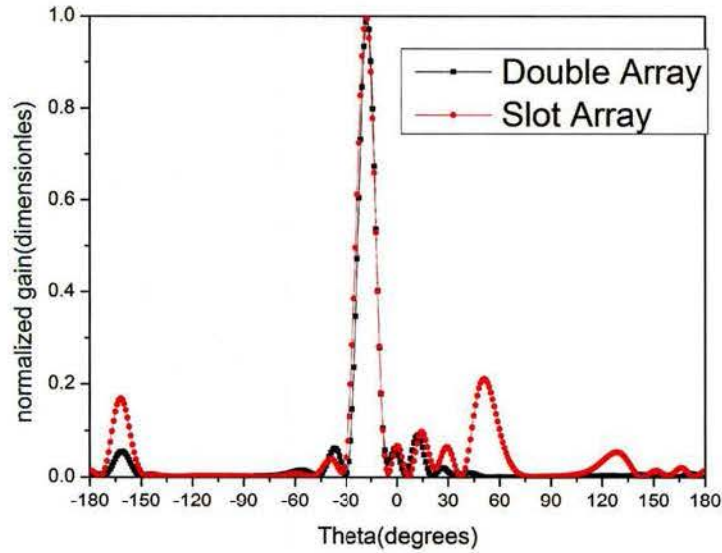
Table I Maximum input power for narrow-wall longitudinal-slot array design in HFSS simulation

	SEA LEVEL	ALBUQUERQUE
Maximum Input Power	2.5 MW	1.8MW

Figures 5 and 6 show further research conducted based on the S-band narrow-wall longitudinal-slot array design. The double-array design presents a low side-lobe level, whereas the circularly polarized antenna presents circular polarization within the range of the main beam.

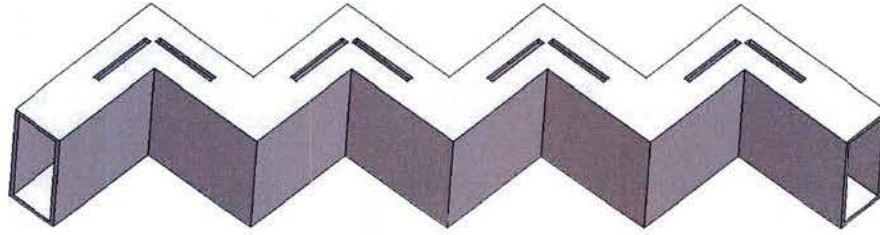


a) Schematic of the double-array

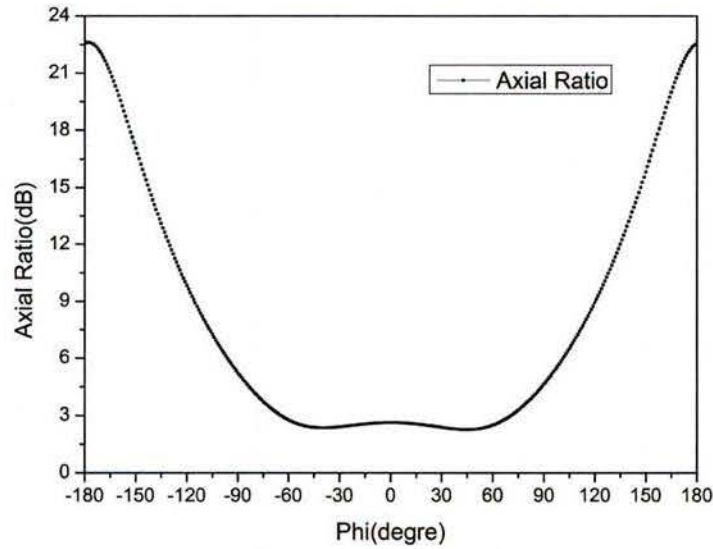


b) H-plane radiation pattern

Figure 5. Schematic and H-plane radiation pattern of double-array design



a) Schematic of the circular-polarized-array design



b) Axial ratio of the circular-polarized-array design in the H-plane
Figure 6. Schematic and axial ratio of circularly-polarized-array design

1.2 Collaboration with NSWC Dahlgren

The University of New Mexico researchers have collaborated with researchers at NSWC Dahlgren, on the fabrication and testing of an S-band narrow-wall longitudinal-slot array waveguide antenna design based on a standard WR340 waveguide. All slots on the narrow-wall of rectangular waveguide were filled with Teflon for better high power handling. Experimental results showed good agreement with the simulation. Figure 7 shows the measured return loss with the input of 700 MW. A return loss of -24.4419 dB at the resonance frequency of 2.86GHz agrees with the simulated results.

Figures 8 and 9 depict the radiation patterns of the S-band narrow-wall

longitudinal-slot array waveguide antenna. The results show good agreement between simulation and measurements.

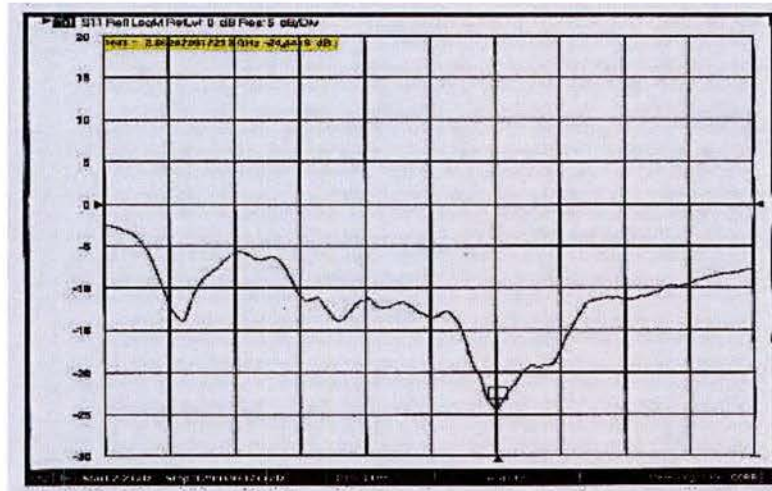


Figure 7. Measured return loss of the S-band narrow-wall longitudinal-slot array waveguide antenna

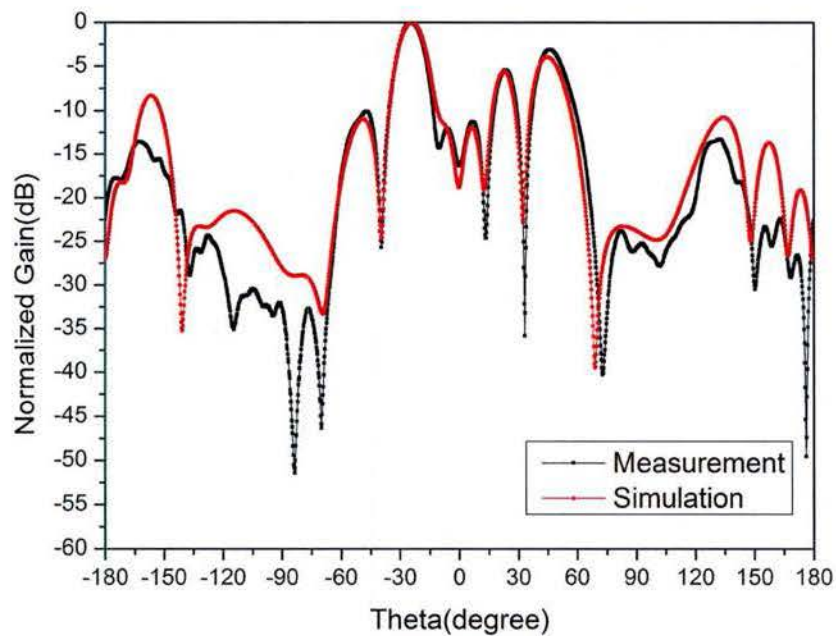


Figure 8. Simulated and measured H-plane radiation pattern of the S-band narrow-wall longitudinal-slot array waveguide antenna

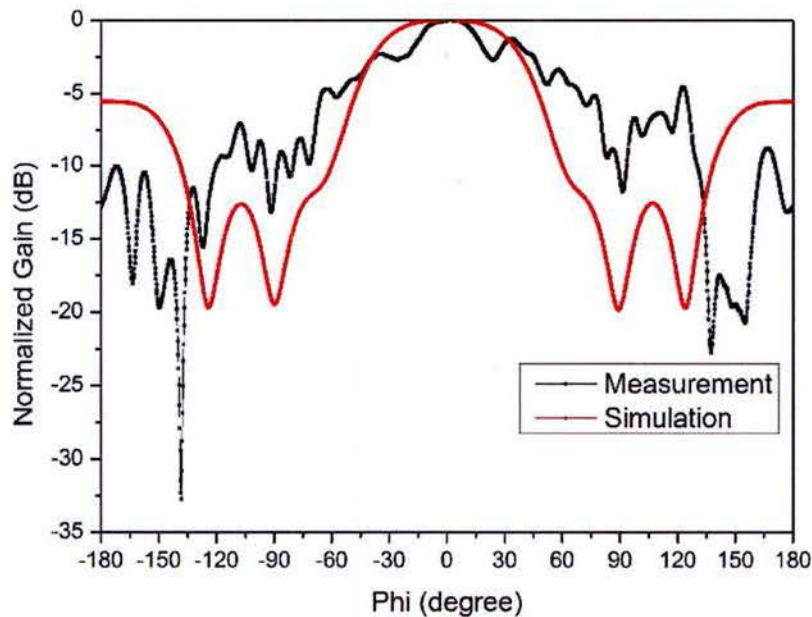


Figure 9. Simulated and measured E-plane radiation pattern of the S-band narrow-wall longitudinal-slot array waveguide antenna

1.3 Collaboration with Air Force Research Laboratory

The University of New Mexico researchers have also collaborated with the Air Force Research Laboratory (AFRL), on testing the S-band narrow-wall longitudinal-slot array waveguide antenna prototype fabricated by the University of New Mexico. The hot test setup for this antenna is shown in the block diagram of Figure 10 as well as in the photographs of Figures 11 and 12.

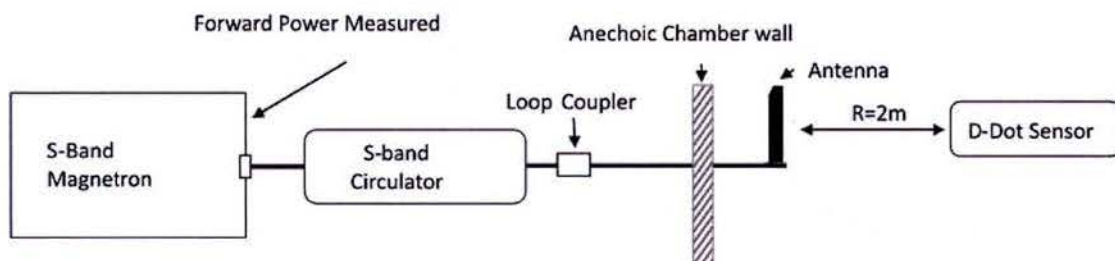


Figure 10. Block diagram of hot test setup

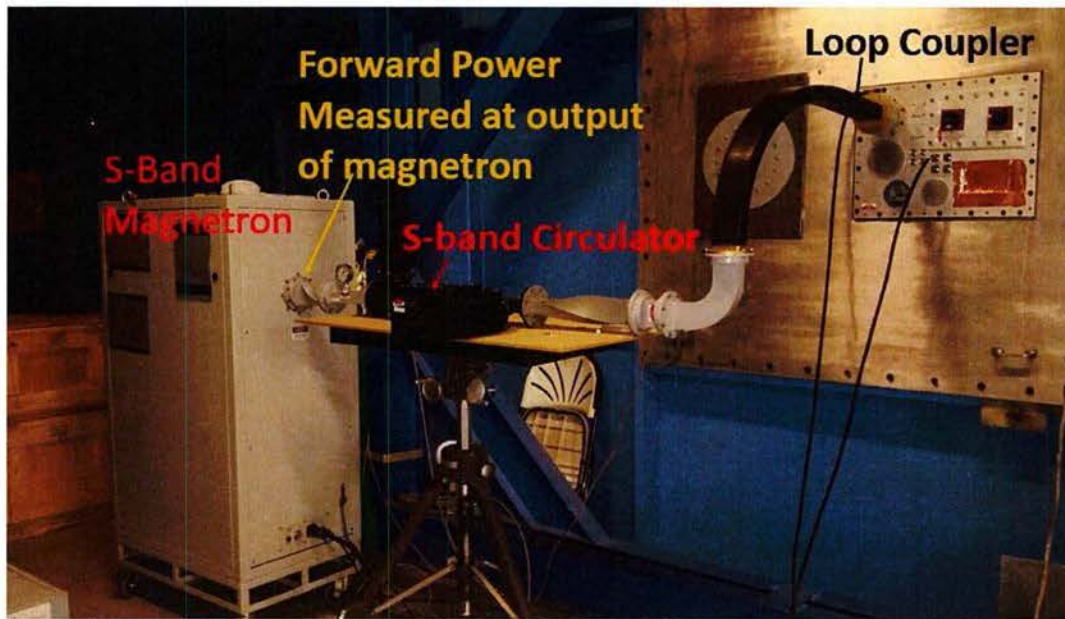


Figure 11. High power microwave source: S-Band Magnetron

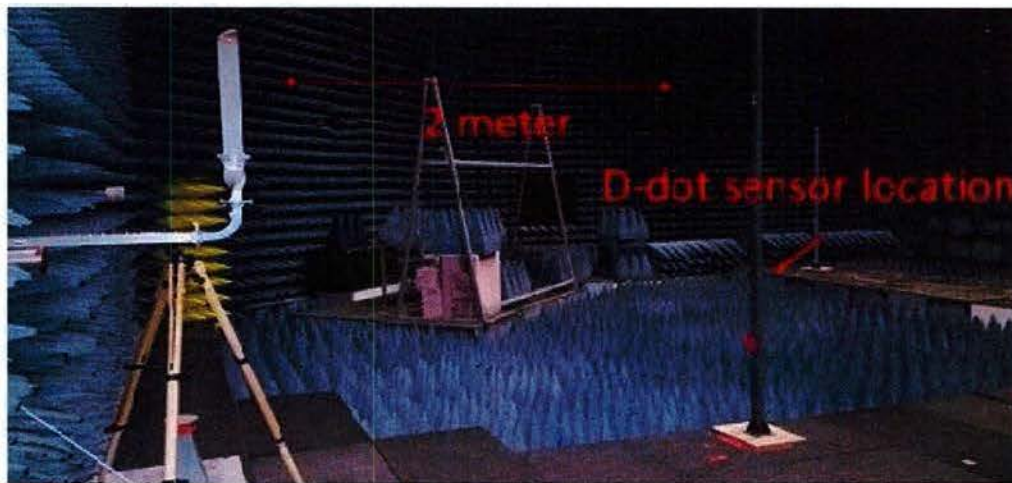


Figure 12. Radiation pattern measurement setup inside anechoic chamber

The S-Band magnetron was located outside of an anechoic chamber as shown in Figures 10 and 11. The source power was fed through a patch panel in the chamber wall via an S-Band waveguide, then connected directly to the antenna inside the chamber. The magnetron used in these tests is tunable in frequency over a limited range. The actual frequency for these measurements was fixed at 3.0 GHz. The magnetron output power was variable from about 200kW up to just over 1 MW. The pulse duration was 500ns. Single pulse field measurements were made using a DDot sensor at a

distance of 2 m from the antenna, in 5 degree increments along an arc in the H-plane as shown in the photograph of Figure 13.

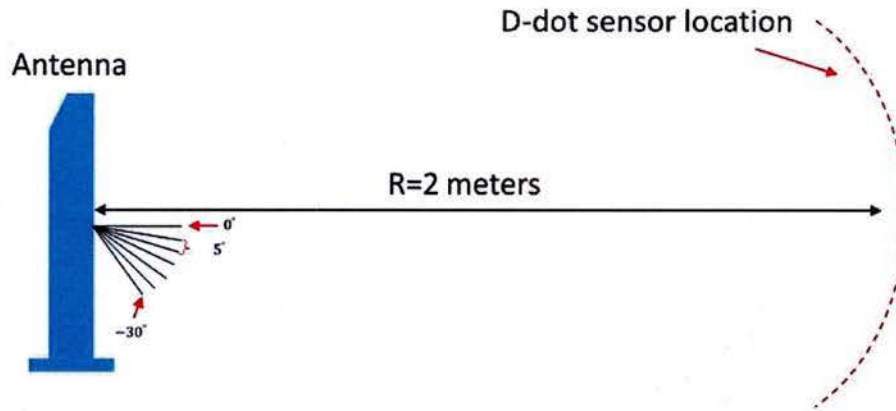


Figure 13. Diagram of H-plane radiation pattern measurements

Table II Measured gain of the antenna within the main beam

Position (degree)	Forward power (W)	Coupler power (W)	Gain (dB)	Simulated Gain (dB)
-5	8.14E+05	7.88E+05	-1.25	-4.52
-10	7.70E+05	7.88E+05	-4.27	2.76
-15	7.60E+05	7.80E+05	9.71	9.59
-20	8.47E+05	8.13E+05	9.91	12.49
-25	7.70E+05	7.88E+05	8.91	10.88
-30	7.70E+05	7.88E+05	-1.59	4.76

Table II presents the measured gain of the antenna within the main beam. Figure 14 shows the comparison of the simulated and measured radiation pattern under large signal experiment. Good agreement were demonstrated. With the input power as high as 0.813MW, no air break-down was observed.

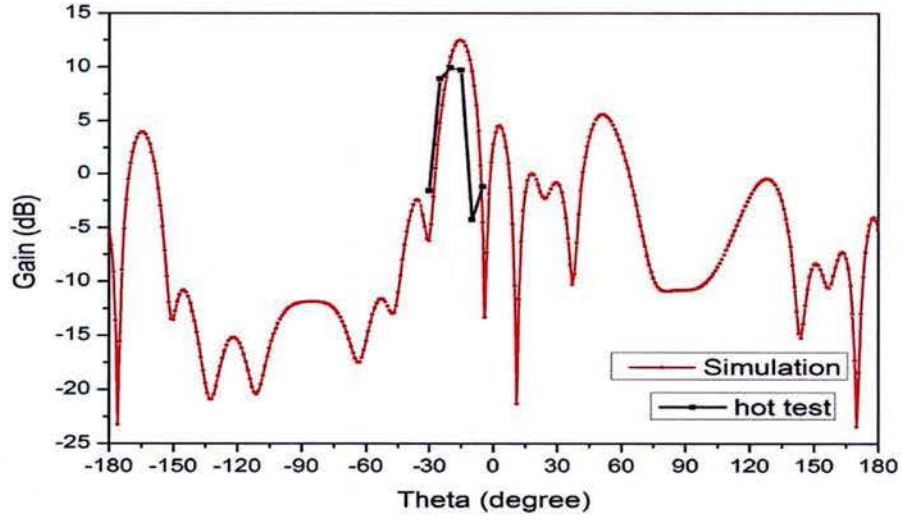


Figure 14. Antenna gain within the main-beam

1.4 Power handling capability estimation for slotted waveguide antennas

Power handling capability estimation determined by air break down (outside the antenna)

The well-known electrical air breakdown value of approximately 3MV/m [19] for static fields, at one atmosphere of air pressure, is used as the upper limit for the maximum allowable E-field values. The air pressure at sea level is approximately one atmosphere, i.e. 760Torr. However, the antenna was tested in Albuquerque, New Mexico, where the air pressure is approximately equal to 627.44 Torr due to its high elevation. From Equation 1.

$$p_h = p_0 e^{-\frac{h}{H}} \quad (1)$$

where

p_h is the air pressure at an elevation of 'h' meters above sea level;

p_0 (=760 Torr) is the air pressure at sea level;

H (=8400 meters) is the approximate scale height of the Earth's atmosphere;

The electrical air breakdown are proportional to the air pressure values, and can be computed through Equation 2 [20].

$$E_{Br}(h) = \frac{p_h \times E_{Br}(0)}{p_0} \quad (2)$$

where

$E_{Br}(0)$ ($=3\text{MV/m}$) is the breakdown E-field value for static fields at one atmosphere air pressure;

p_h is the value of the air pressure between the values of 260 Torr and 760 Torr;

$E_{Br}(h)$ is the breakdown E-field value for static fields at an air pressure of ' p_h '.

The corresponding air breakdown value in Albuquerque is computed from Equation 2 and it is approximately equal to 2.48MV/m . The computational software ANSYS-HFSS was used to monitor the near-field radiation of the S-band longitudinal slotted waveguide antenna driven by various input power levels, as shown in Figure 15. Note, the value of the maximum E-field in the center of first slot is exactly linear to the square root value of the input power. Such values were recorded and used to determine the maximum input power, as shown in Table III.

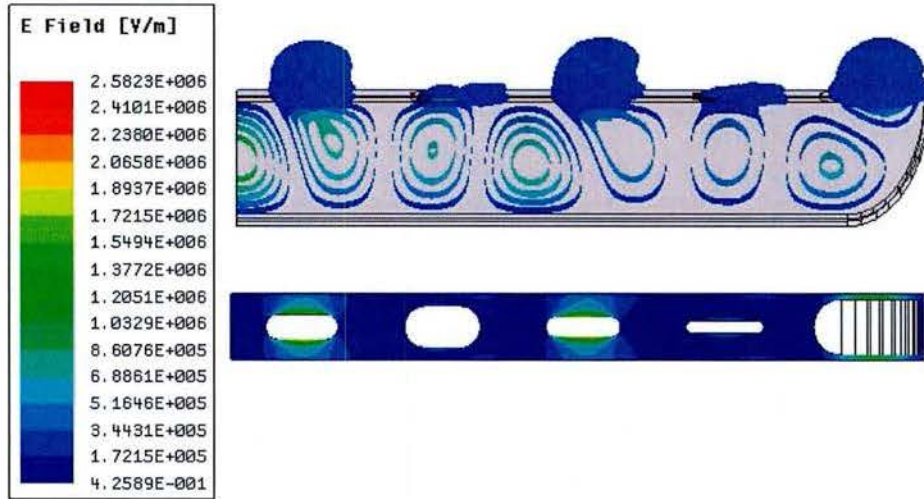


Figure 15. E field distribution simulated by HFSS

Table III Input power vs maximum E-field value by HFSS

Input power (W)	1E3	1E6	1.8E6	10E6
E_{\max} (V/m)	5.67E4	1.89E6	2.4E6	5.67E6

For the S-band longitudinal slotted waveguide antenna operating at 3.17GHz in Albuquerque, NM, U.S., an input power of approximately 1.8MW through the S-band feed-waveguide would produce electrical field stronger than the threshold of 2.48MV/m, thus causing air breakdown.

Power handling capability estimation determined by multipaction (inside the antenna)

Multipaction is an RF vacuum breakdown mechanism, where an electron avalanche-like discharge occurs in structures operating under vacuum conditions and high-power electromagnetic fields [21]. When the intensity of the applied field is such that the electrons bombarding the walls have kinetic energy high enough, then secondary electrons may be released from the walls. If this process sustains itself, causing continuous growth of the electron population inside the device then we get the multipaction effect.

The electron population is expected to grow until a steady-state (saturation level) is reached [22]. Previous numerical simulations presented in [23] show that the saturation level is within the range of 10^9 - 10^{12} electrons between two parallel metal plates separated by 1mm, depending on the particular characteristics of the case (waveguide dimensions, SEY (secondary electron yield) properties, RF voltage). In the study of the S-band slotted waveguide antenna, we chose the saturation level of N_{sat} to be 10^{15} . After trying different levels of N_{sat} , we noticed that the aforementioned value is the best one to fit the experimental data.

The computational software CST Particle-in-cell Solver was used to analyze the S-band narrow-wall longitudinal slotted waveguide antenna. The material chosen was copper (ECCS: European Cooperation for Space Standardization). It follows a SEY curve based on the Furman model [24], which also provides the energy and angular distribution for the emitted electrons, while the Vaughan model [25], frequently used in the microwave industry, provides only a SEY curve.

In a typical multipactor breakdown analysis/estimation, the time frame of the operation is long enough that whenever the speed of the growth of the particles surpasses exponential growth, the population of the particles will eventually reach the saturation level. However, for the case of the relatively long pulse duration in our simulation/experiment, there's no guarantee that the population of the free electrons will reach the saturation level. This requires a full simulation over the entire operation time frame which increases the complexity of analysis.

To better predict the threshold of the multipaction power level and to reduce simulation time, a classic quick input power threshold estimation was performed within a simulation duration of 20ns. The result is shown in Figure 16. First, there's no multipaction around 800kW and it's quite clear that the threshold should be somewhere between 1.5MW and 3MW. Further investigations over a much longer time frame are needed to determine the input power threshold.

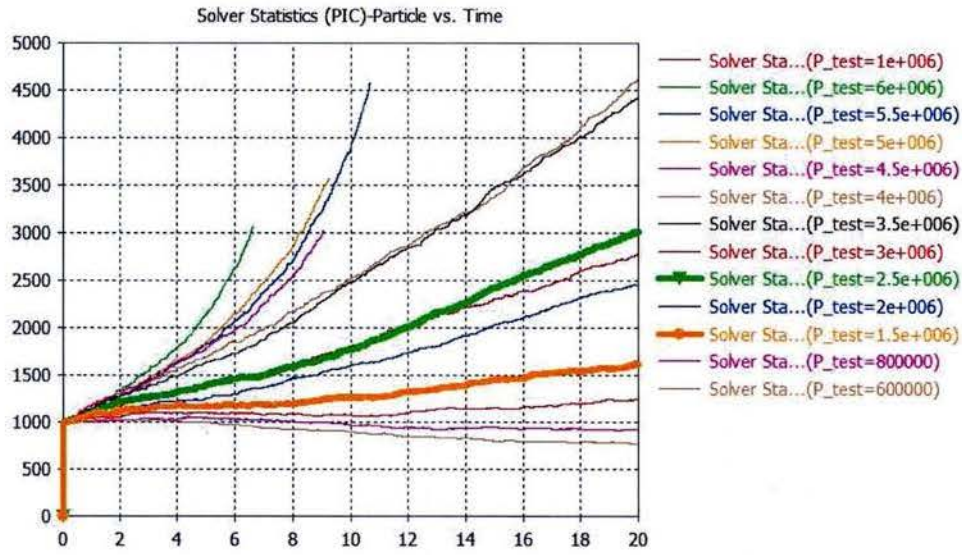


Figure 16. Power threshold estimation by CST

We choose the input power to be 2.35MW, 2.54MW and 2.75MW, respectively for further estimation. Figure 17 shows the number of electrons inside the antenna as a function of time. The simulation times are 45 minutes, 45 hours and 85 hours, respectively.

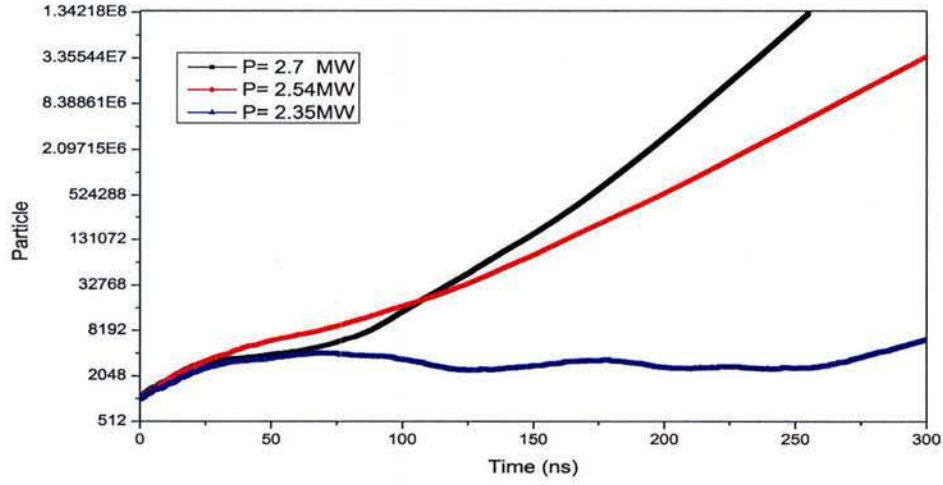


Figure 17. Number of electrons inside the antenna for input power of 2.35MW, 2.54MW and 2.75MW

None of the cases simulated above present a rapid exponential growth of particle population beyond a base of 1.07. Table IV shows the estimated particle population.

Table IV Population of electrons under varies input power

Input power (mW)	2.35	2.54	2.75
N (t=300ns)	6E4	3.5E7	1.1E8 (t=250ns)
Projected N	6E10	2.6E14	2.5E16 (t=500ns)

When the antenna is excited with input power of 2.75MW, the particle population is projected to reach the saturation level of 10^{15} 500ns. And for input power up to 2.35MW, the particle population is far from reaching the saturation level. Figure 18&19 show the distribution of the electrons at T=300ns for an input power of 2.35MW and 2.54MW. Due to the restriction of computer hardware, a full simulation of 500ns is almost impossible. We predict the input power threshold for the S-band narrow-wall longitudinal slotted waveguide antenna, before multipaction, to occur inside the antenna around 2.54MW input power, based on simulations of duration of 300ns.

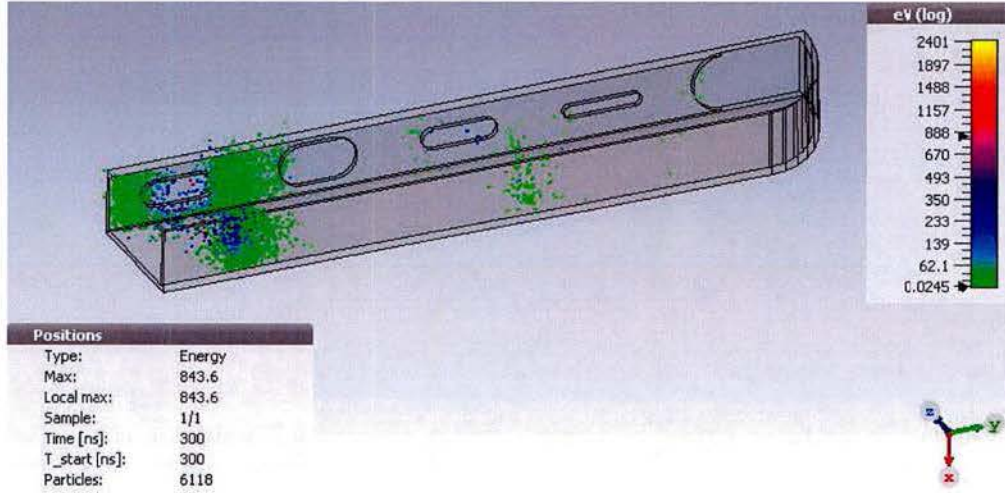


Figure 18. Distribution of the electrons inside the antenna ($P_{in}=2.35\text{MW}$)

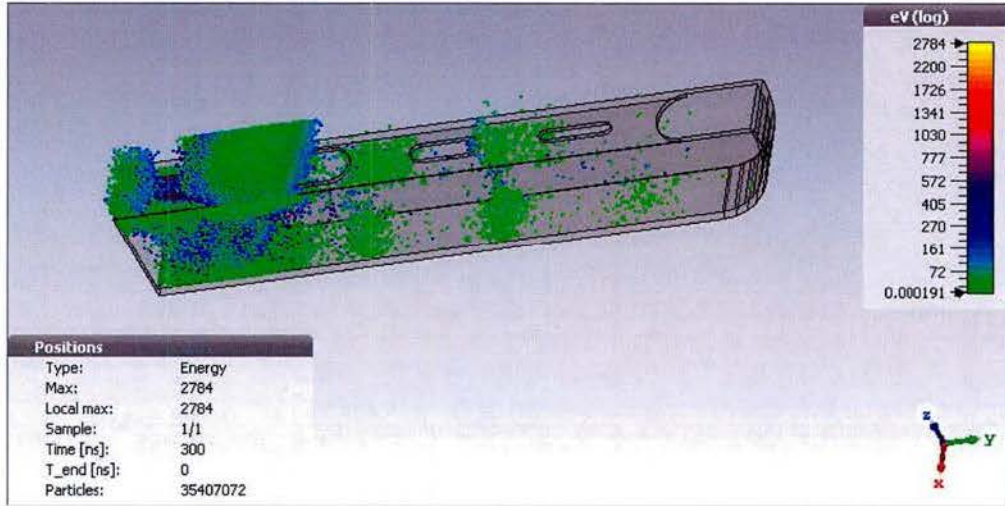


Figure 19. Distribution of the electrons inside the antenna ($P_{in}=2.54\text{MW}$)

2. Miniaturization of narrow-wall slotted waveguide antenna designs

2.1 Periodic structures applied for antenna miniaturization and beam-steering

Split-ring-loaded waveguide:

Periodic structures such as split-ring-resonators have been applied to our waveguide antenna design as metamaterials, exhibiting properties such as backward travelling wave in the waveguide. A reduction in the cross section of the slotted-waveguide antenna was achieved by inserting an SRR array into a standard rectangular waveguide, supporting the antenna operating under cut-off frequency. Figure 20 shows the

schematic of the H-plane-bend radiator loaded with an SRR-array. Figure 21 presents the amplitude and phase of S_{11} of the H-plane-bend radiator loaded with an SRR-array. A sudden increase in phase indicates back-ward wave travelling inside such waveguide structure. Figure 22 shows the co-polarized and cross-polarized components of the H-plane-bend radiator loaded with an SRR-array, which is identical to the original HPB radiator.

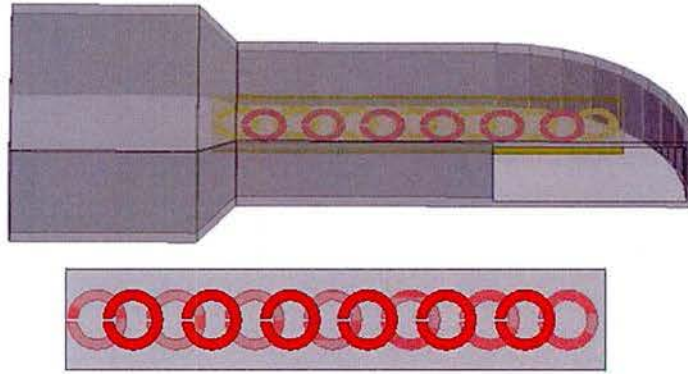


Figure 20. Schematic of HPB-radiator loaded with an SRR-array (overlapping placement of rings)

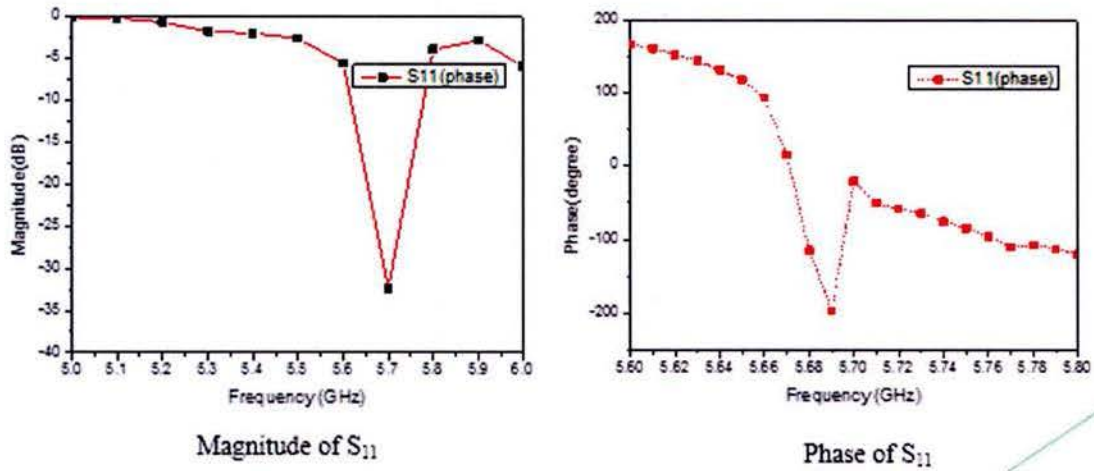


Figure 21. S_{11} of H-plane-bend radiator loaded with an SRR-array

The results showed how periodic structures such as SRR-arrays can be applied to the H-plane-bend radiator, which is a key part of the narrow-wall longitudinal-slot array design. Approximately, a 60% transverse aperture reduction was achieved.

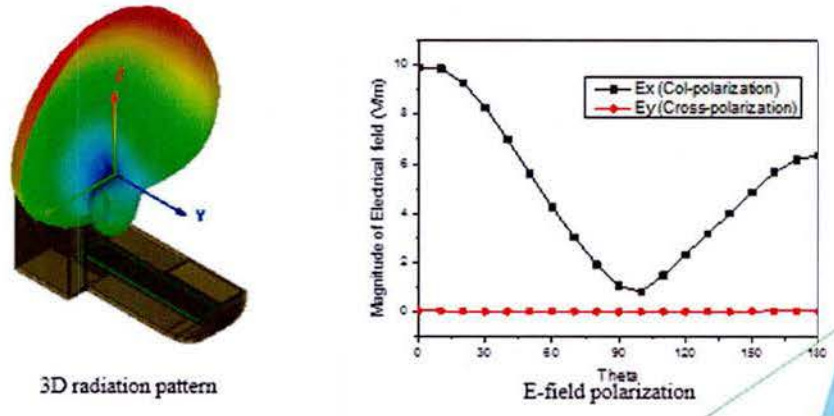


Figure 22. 3D radiation pattern & E-field polarization of HPB-radiator loaded with an SRR array

Extending the SRR-array design to the narrow-wall, the longitudinal-slot side, further miniaturization can be achieved while maintaining a high-gain, low sidelobes and good return loss. A non-uniform SRR-array was also investigated to meet the design goals. Moreover, other periodic structures such as corrugations and stubs on the broad-wall and the narrow-wall sides of the waveguide were considered.

Double narrow-wall longitudinal-slot array waveguide antenna:

To further reduce the side lobe level of the original HPM antenna a new design, based on a double narrow-wall longitudinal-slot array waveguide antenna, shown in Figure 23, was studied. A new feeding network based on a composite right-hand/left-hand (CRLH) waveguide structure was proposed as well to achieve beam-steering.

The goal of the experiment was to show that the antenna with the proposed feeding network can achieve beam-steering by mechanically varying the length of stubs in CRLH waveguide structures.

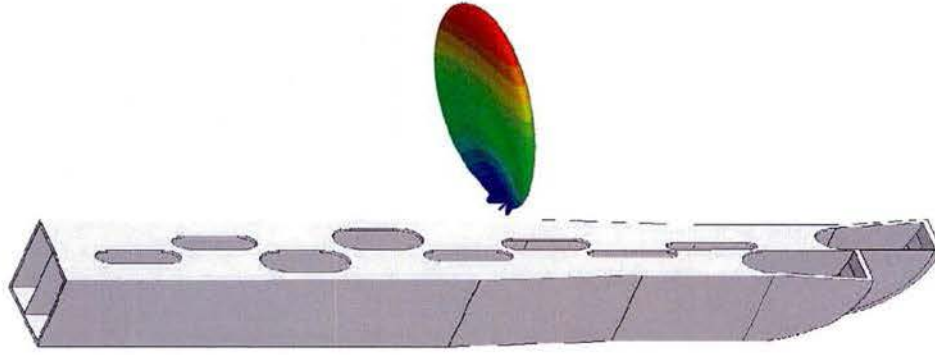


Figure 23. Schematic of double narrow-wall longitudinal-slot array waveguide antenna and its 3D radiation pattern

Figure 23 also shows the simulated radiation pattern of the double narrow-wall longitudinal-slot array waveguide antenna. The proposed design indicates a peak gain of 14.9 dB with a side-lobe level of -10.7 dB.

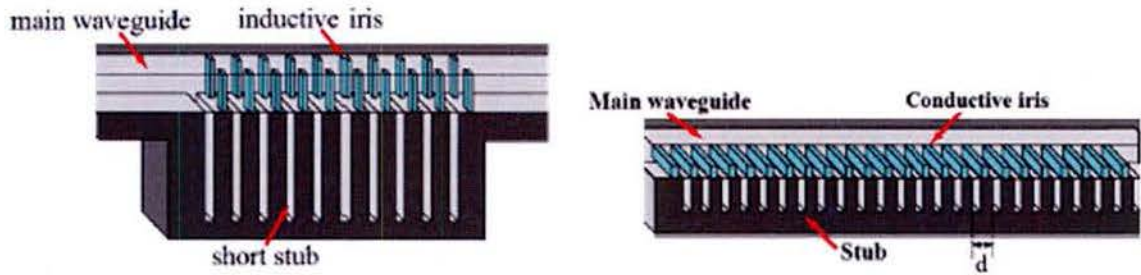


Figure 24. Configuration of CRLH waveguide structure

Figure 24 shows the configuration of the CRLH waveguide structure. The left-handed waveguide is composed of periodic structures as the pair of an inductive iris for shunt inductance and a short stub longer than a quarter wavelength for series capacitance. The delay line of the right-handed waveguide is achieved by a capacitive iris for shunt capacitance and a short stub, shorter than a quarter wavelength for series inductance. Varying the length of the stubs provides different phase at the output. The output of such feeding network will be connected to the input of two input ports of the double narrow-wall longitudinal-slot array waveguide antenna design, respectively.

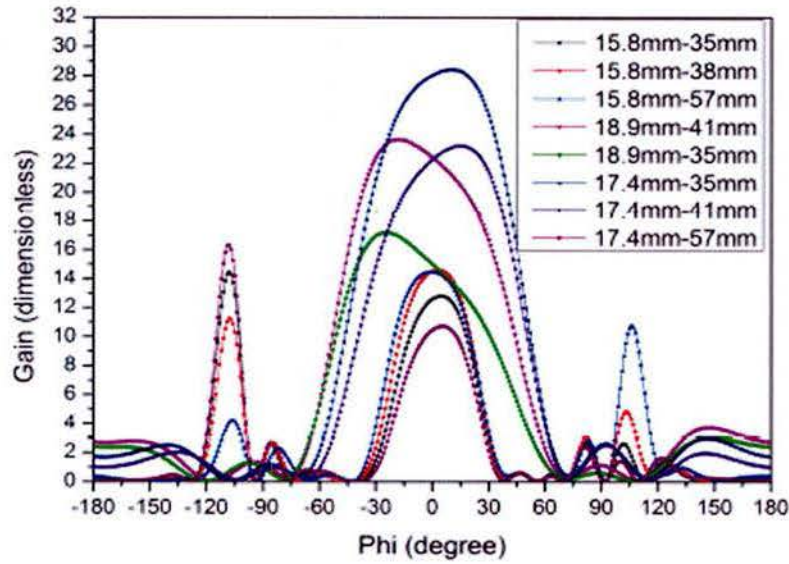


Figure 25. Azimuth plane radiation pattern for different lengths of short stubs of left-handed/right-handed waveguide

Figure 25 shows the predicted beam-steering by varying the length of the stubs in the CRLH waveguide structures. Though the feeding network has a -3dB transmission loss, it proved to be an efficient way to properly feed the double narrow-wall, longitudinal-slot array waveguide antenna, and perform high power beam-steering.

2.2 A Compact S-band narrow-wall complementary-split-ring slotted waveguide antenna

In this section a compact S-band narrow-wall complementary-split-ring slotted waveguide antenna is proposed for further antenna size reduction while maintaining similar radiation characteristics as the longitudinal slotted waveguide antenna. The antenna model was fabricated and tested.

Complementary-split-ring slots in the narrow-wall of a rectangular waveguide

In order to reduce the slot size of conventional half-wavelength slotted waveguide antennas, complementary-split-rings slots in the narrow-wall of a rectangular waveguide was introduced for the first time.

The parameters that define the geometry of the CSR slot are shown in Figure 26. The waveguide used in this study is a standard S-band waveguide, WR284. The outer radius of the outer ring is defined by R , the width of both the inner and outer rings is defined by w , and the size of the gaps in the split section of both the inner and outer rings is defined by d or α . The gap between the inner radius of the outer ring and the outer radius of the inner ring is defined by g_{sr} . The rotation of the inner and outer split ring around its center relative to the waveguide centerline are set to be -90° and $+90^\circ$, respectively. These rotation angles are chosen to intercept the surface current on the narrow-wall.

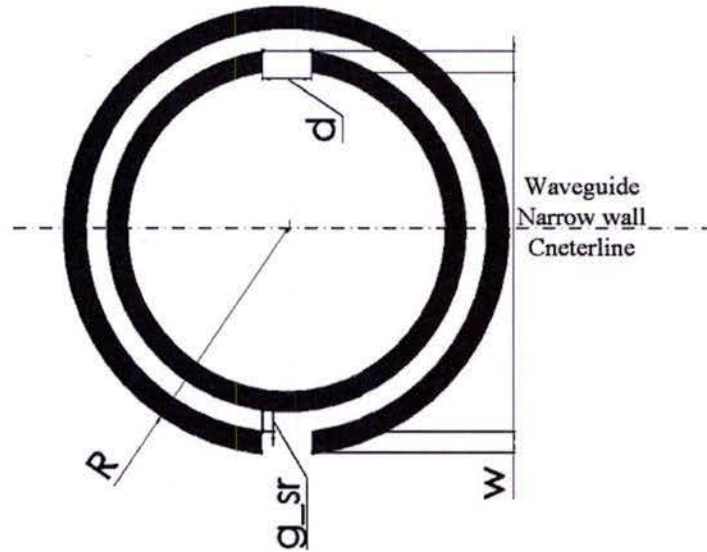


Figure 26. Design parameters of the CSR slot

The resonant frequency of the CSR-slot can be independently controlled by parameters R , w , α . The resonant frequency of the CSR slot mainly depends on its circumference. Thus, as shown in Figure 27 for the S11, increasing R while keeping w , α and g_{sr} constant results in the reduction of the resonant frequency. Similarly, Figure 28 shows that increasing the circumference of the split ring by reducing α leads to a reduction of the resonant frequency. The capacitance of the split ring is reduced by increasing w which consequently increases the resonant frequency of the CSRR. However, the inductance of the split ring increases by increasing w which reduces the resonant frequency.

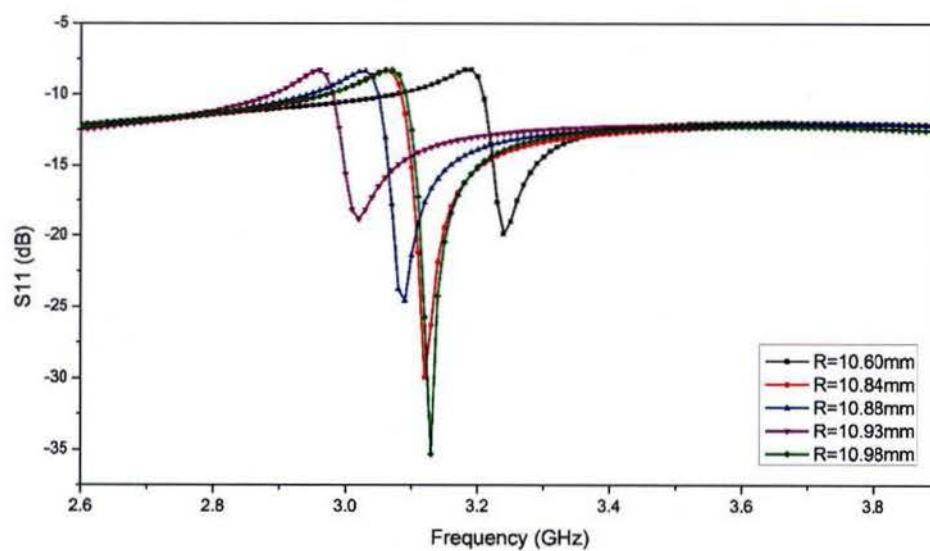


Figure 27. S_{11} vs R

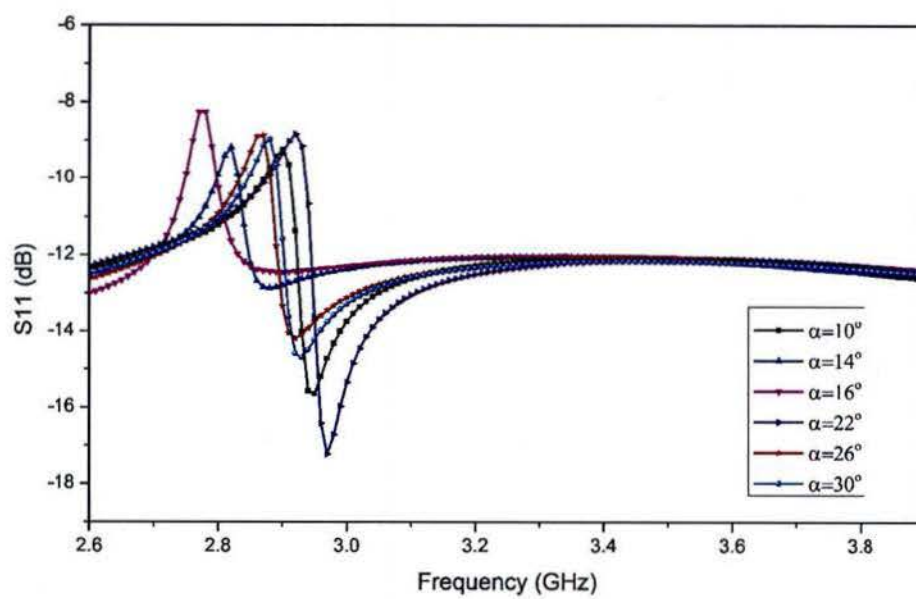


Figure 28. S_{11} vs α

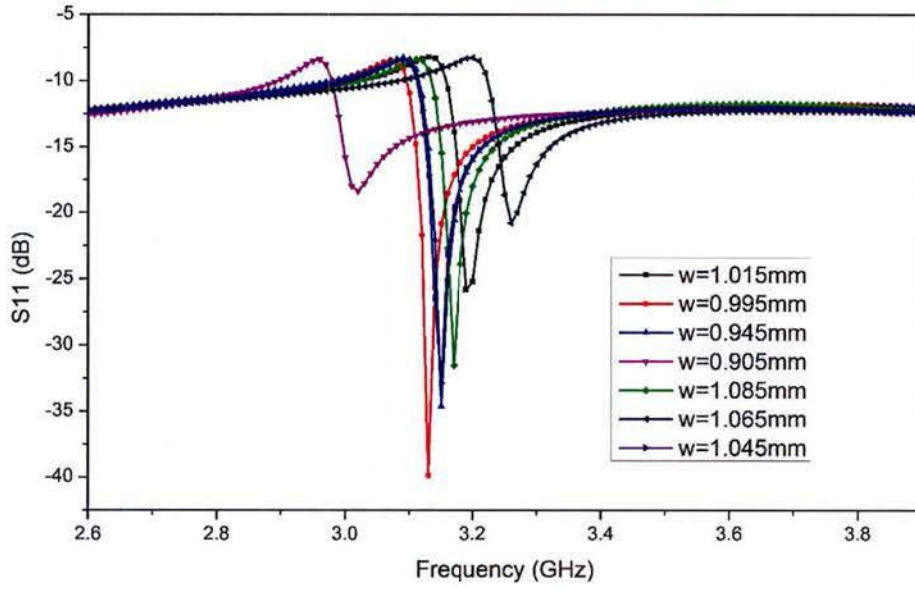


Figure 29. S11 vs w

The effective capacitance of the split ring is a factor of the ratio of the inner and outer radii of the ring and this ratio depends on w as well. However, the effective inductance depends on the square value of the gap width. Therefore for a constant R , α and g_{sr} , the resonant frequency of the split ring slot can further be reduced by increasing w .

In general, the sensitivity of these parameters on the overall properties of a CSR-type antenna increase the difficulty of modeling the CSR-slots compared to the standard longitudinal slots. In the case of longitudinal slots, for a specific width, there is a corresponding length that produces resonance or peak power radiated, and sharper resonances are associated with thinner slots, while in the case of CSR-slots, it's the specific set of R , W , α , g_{sr} contributing to resonance or peak power radiated.

Microwave network analysis

To maximize the peak directivity of the array, the elements of the array are designed to radiate equal power and possess a constant progressive phase shift so that the design forms a uniform array. In order to minimize the power reflected into the feed-waveguide, the power reflected into individual elements need to result in

destructive interference. The optimal single-array design is a trade-off between minimizing the reflected power at the input of the array and designing a perfect uniform array for radiation purposes.

Ideally, a matched load is preferred at the end of the waveguide instead of a shorting cap, to reduce the power reflected to the feed. An unmatched load might also generate a secondary canted beam from the broadside direction due to the wave reflected from the load. Thus, the HPB-radiator is a perfect fit for slotted waveguide antenna designs since it serves as a matched load and a radiating element at the same time. For an operating frequency of 3.1689GHz, the optimal length of the HPB-radiator is 47.335mm ($\lambda/2$), while the width of the HPB-radiator is the same as the width of the standard rectangular waveguide WR284, 34.04mm. The number of elements in the single array is set to be five, to compare the design to the S-band longitudinal slotted waveguide antenna reported in Section II-1.1.

The idea of reducing the array design to a microwave network analysis that was introduced in [], is applied in this analysis as well. The equivalent microwave network for the single array is shown in Figure 3.2. This approach is based on the assumption that the external coupling between the array elements is negligible, which is acceptable in the case of the longitudinal slot array, where the inter-element spacing is $11/16\lambda_g$. However, such an assumption requires further validation in this CSR-slot study. Due to the much more compact slot size, the inter-element spacing can be reduced significantly. However, this means much stronger mutual coupling between the slots, which needs to be considered during the design process. Also, the CSR-slots are resonant structures, with very narrow bandwidth, and any interruption (i.e. mutual coupling from other slots) might result in a shift in resonant frequency, which consequently alters the S parameters of the slots.

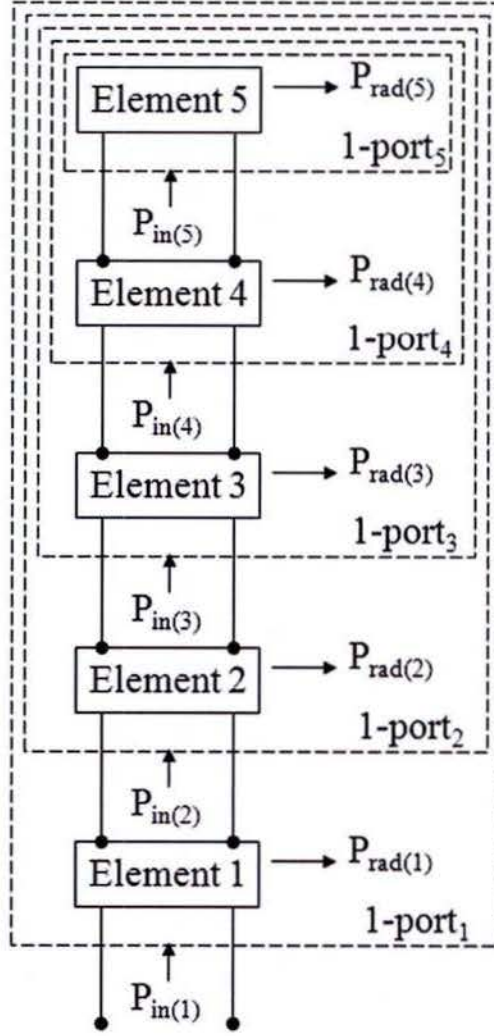


Figure 30. Equivalent microwave network of the slot array

Each CSR-slot is represented as a lossy 2-port network (slot 1 to 4) and the HPB-radiator is represented as a lossy 1-port network. The power radiated by each slot (including the HPB-radiator) is represented by the loss in the corresponding network. The power radiated by slot n is defined as $P_{rad}(n)$, where n takes the integer number of 1 to 5. The power input to the n th lossy network is defined as $P_{in}(n)$. The reflection coefficient of the n th lossy network is defined as Γ_n . The power accepted by the n th lossy network is defined as $P_{load}(n)$, and is represented in.

$$P_{rad}(n) = P_{in}(n)(1 - |\Gamma_n|^2) = \sum_{m=n}^5 P_{rad}(m) \quad (3)$$

As a perfect uniform array, each element radiates equal power ($0.2P_{in}(n)$, in the case of 5 elements array). Ideally, the optimal values of the ratio of the radiated power ($P_{rad}(1)$ through $P_{rad}(5)$) to the input power ($P_{in}(1)$ through $P_{in}(5)$) are given by $0.2P_{in}(1)$, $0.25P_{in}(2)$, $\frac{1}{3}P_{in}(3)$, $0.5P_{in}(4)$, $P_{in}(5)$, respectively. Expressions for $P_{rad}(1)$ through $P_{rad}(5)$ and Γ_n , in Figure 30 are obtained in terms of the S-parameters of the array elements, inter-element spacing, and $P_{in}(1)$ using standard microwave network analysis.

$$\Gamma_n = S_{11} + \Gamma_{n+1}S_{12}\left(\frac{S_{21}}{1-\Gamma_{n+1}S_{22}}\right) \quad (4)$$

$$P_{in}(n) = P_{in}(n+1) \left| \frac{1-\Gamma_{n+1}S_{22}}{S_{21}} \right|^2 \quad (5)$$

$$\sum_{m=n}^5 P_{rad}(m) \quad (6)$$

An important assumption is made that if the array of CSR-slots and the array of longitudinal half-wavelength slots can be characterized as the same microwave network, the radiation properties of both arrays should be similar, if not identical. This assumption is based on the parametric study of the CSR-slots and radiation characteristics of the CSR-slots, which show similar total efficiency, gain and polarization as well as radiation patterns to the conventional longitudinal slots. This assumption was further validated using numerical full-wave analysis.

Based on this assumption, the inter-element spacing is set to be $11/16\lambda_g$, so that the design of the S-band longitudinal narrow wall slot array can be applied, as shown in Figure 31. Using the optimal values of $P_{rad}(1)$ through $P_{rad}(5)$, and the corresponding S parameters of each microwave network, the optimal dimensions for CSR slot 1 to 4 were derived as shown in Table V.

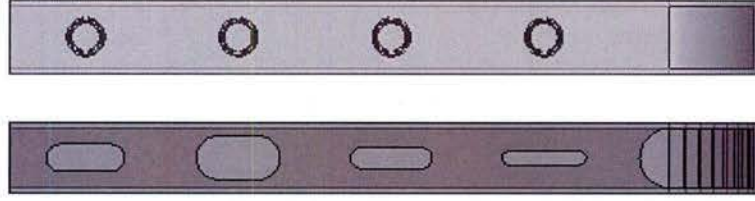


Figure 31. Comparison of the CSR-SWA with the longitudinal slot array (same inter-element spacing)

Table V Results from microwave network analysis

Element	R/mm	w/mm	g_{sr}/mm	$\alpha/^\circ$
slot 1	10.828	1.029	1	15.0
slot 2	10.842	0.955	1	14.9
slot 3	10.842	1.029	1	14.9
slot 4	10.842	1	1	14.8

Narrow-wall complementary-split-ring slotted waveguide antenna

An S-band narrow-wall complementary-split-ring slotted waveguide antenna was also designed for high-power-microwave applications. The proposed antenna operates at 3.17GHz with a return loss of -30dB. Figure 32 shows the schematic of the S-band narrow-wall complementary-split-ring slotted waveguide antenna. The antenna design uses an inter-element spacing of $0.2875\lambda_g$, thanks to the much smaller CSR-slot size. However, it's a tradeoff between the reflected power, antenna miniaturization and radiation performance of the antenna, like gain, main beamwidth, sidelobe level, etc.

An experiment was conducted with a standard S-band WR-284 waveguide as the feed guide. The manufacturing of the complementary-split-ring slots on a metal plate is more difficult than that of the standard rectangular waveguide of circular slots. Waterjet cutting was used to create the CSR slots on an aluminum plate. The aluminum plates used have a thickness of 0.125in, thicker than standard rectangular waveguide WR284 walls. Figure 33 shows the four aluminum plates fabricated and the complementary-split-ring slotted waveguide antenna. The final product was achieved

by welding those four aluminum plates together.

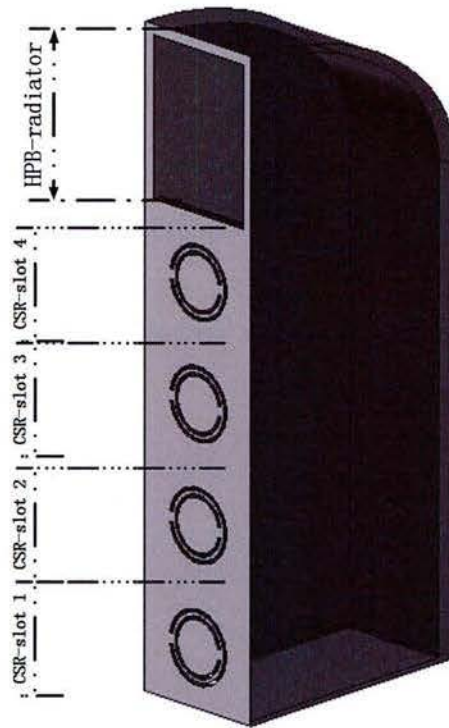


Figure 32. Schematic of the CSR-SWA



Figure 33. Aluminum plates fabricated by Waterjet Cutting

Measurements show that the antenna provides a fan-beam radiation pattern, as predicted by HFSS simulations. Figure 34 presents simulated and measured return loss

results of the S-band narrow-wall complementary-split-ring slotted waveguide antenna. Figure 35 shows the comparison of the S-band narrow-wall complementary-split-ring slotted waveguide antenna and the S-band narrow-wall longitudinal-slot array waveguide antenna.

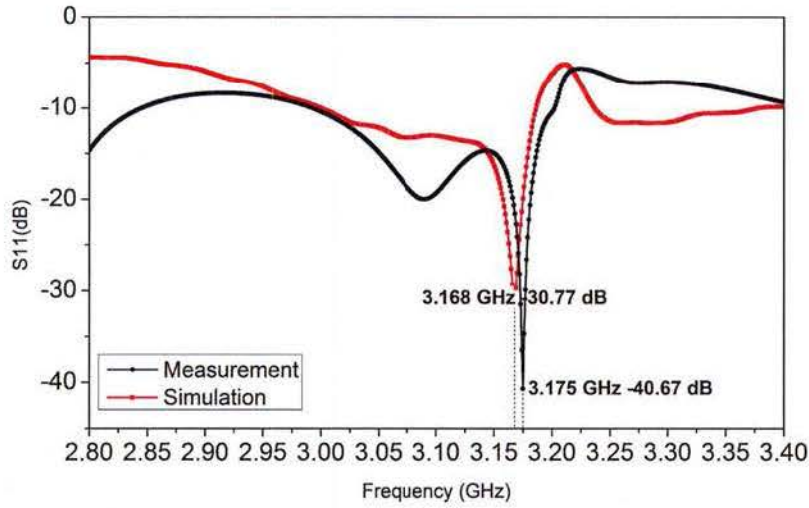


Figure 34. Simulated and measured S11 of the CSR-SWA



Figure 35. Comparison of the CSR-SWA and the longitudinal SWA

Figure 36 shows the radiation pattern measurement set-up at University of New Mexico, and Figure 37 depicts the simulated and measured radiation pattern of the narrow-wall

complementary-split-ring slotted waveguide antenna.

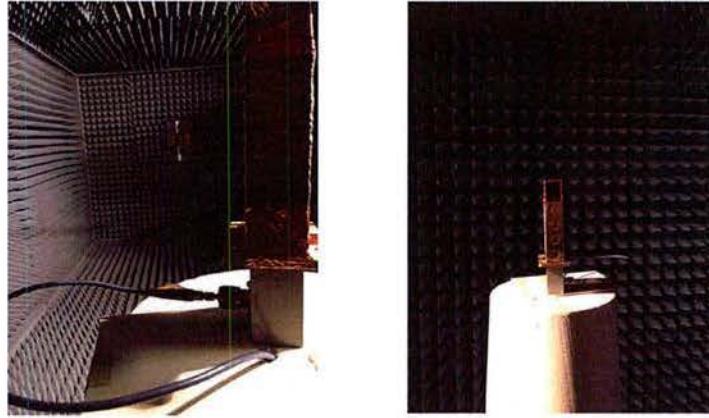


Figure 36. Radiation pattern measurement set-up for the CSR-SWA

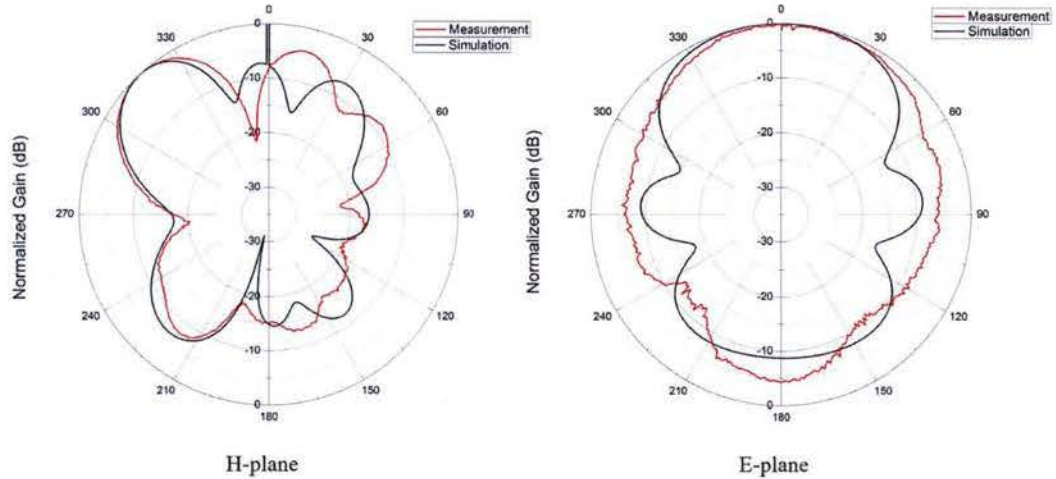


Figure 37. Measured & simulated normalized radiation pattern of the CSR-SWA

Complementary-split-ring slotted waveguide antenna loaded with periodic air-filled corrugations

Due to the thick walls used, a set of periodic air-filled corrugations is added to the opposite narrow-wall of the rectangular waveguide, to further enhance the coupling between the wave propagating along the waveguide and the much deeper CSR slots.

Figure 38 shows the basic schematic of the periodic air-filled corrugations added to the waveguide, which start at the input and end right before the HPB-radiator. The height, length and inter-spacing of the periodic corrugations were optimized to enhance the

coupling between the wave inside the waveguide and the CSR slots, which results in higher peak antenna gain.

Figures 39 and 40 show the simulated radiation patterns of the narrow-wall CSR-SWAs loaded with periodic air-filled corrugations, compared to the narrow-wall CSR-SWAs without corrugations.

It is apparent that the complementary-split-ring slotted waveguide antenna has the advantage of being *more compact* compared to the conventional half-wavelength longitudinal slot array and has *better radiation performance* (i.e. higher gain, narrower beamwidth) compared to the conventional quarter-wavelength longitudinal slot array.

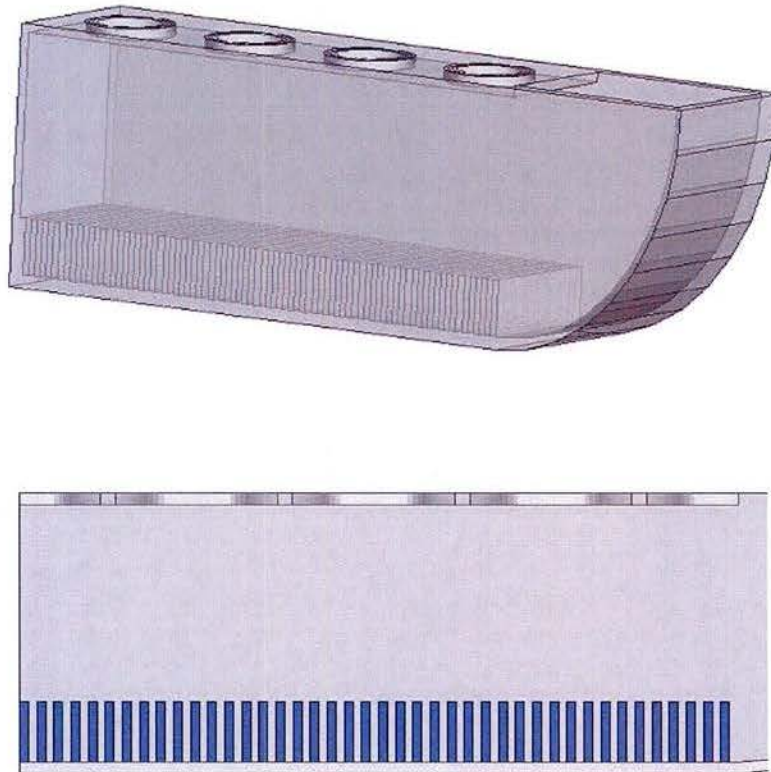


Figure 38. Periodic corrugations added to the other narrow-wall of the CSR-SWA

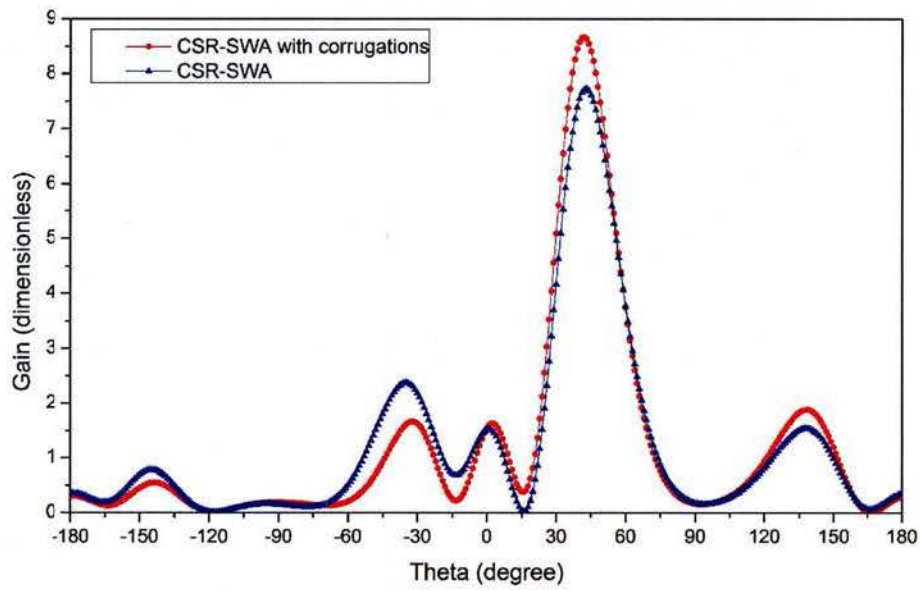


Figure 39. H plane radiation pattern of the CSR-SWA and the CSR-SWA loaded with corrugations

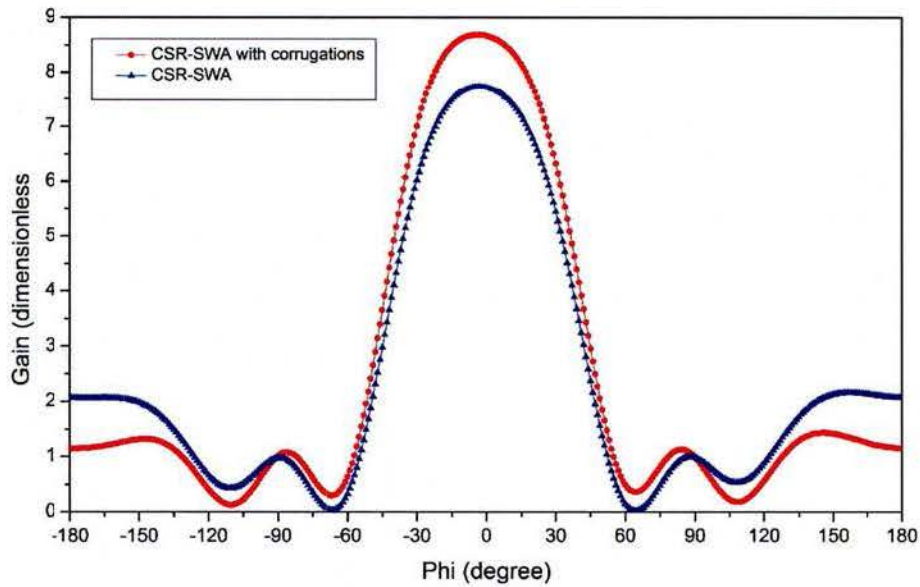


Figure 40. E plane radiation pattern of the CSR-SWA and the CSR-SWA loaded with corrugations

Complementary-split-ring slotted waveguide antenna array

An array of two CSR-SWAs attached to each other is shown in Figure 41. This configuration can suppress the grating lobe level of the longitudinal slotted waveguide

antenna. The array consists of two CSR-SWAs placed next to each other. The CSR slots are placed so that the apertures alternate from one side of the attached broadwall to the other. The two CSR-SWAs are fed with equal power and a phase difference of 6.5° .

Figure 42 and 43 show the gain radiation pattern of the array compared to the single longitudinal slotted waveguide antenna. The array clearly provides a narrower main beam and lower side-lobe level. The peak gain of the array is 11.75dB, very close to the peak gain of the single longitudinal slotted waveguide antenna (12.4dB).

The CSR-SWA array provides a higher gain than the single CSR-SWA and reduces the grating lobe level which is significantly higher in the case of the single CSR-SWA than in the case of the longitudinal SWA. Figures 44 and 45 show the normalized radiation pattern of the array compared to the single CSR-SWA.



Figure 41. Schematic of the CSR-SWA double array

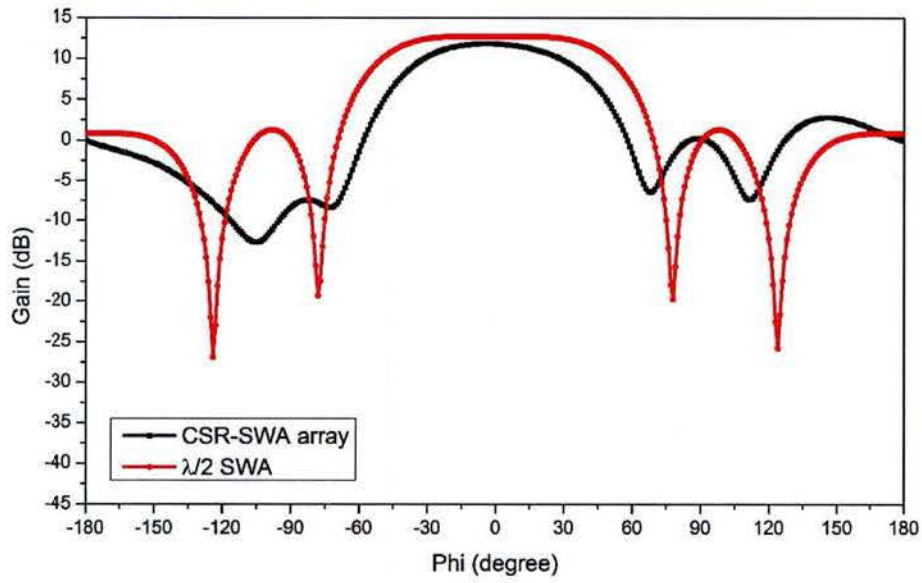


Figure 42. E-plane radiation pattern of the CSR-SWA double array and the longitudinal slotted waveguide antenna

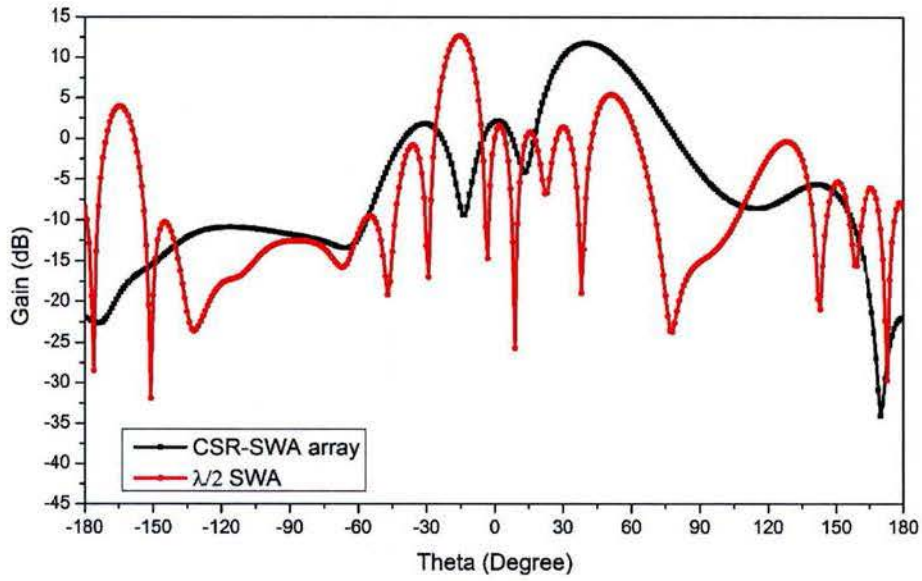


Figure 43. H-plane radiation pattern of the CSR-SWA double array and the longitudinal slotted waveguide antenna

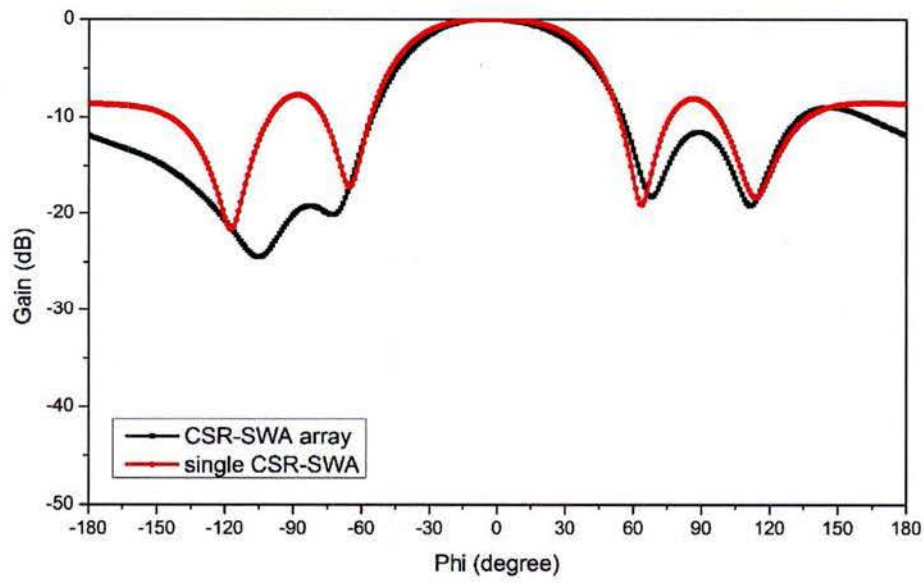


Figure 44. Normalized E-plane radiation pattern of the CSR-SWA double array and the single CSR-SWA

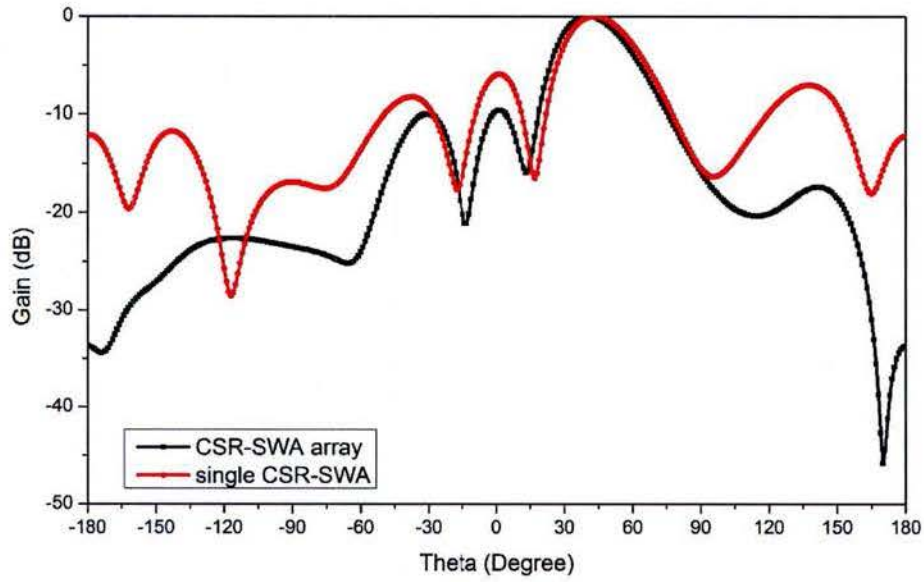


Figure 45. Normalized H-plane radiation pattern of the CSR-SWA double array and the single CSR-SWA

The conclusion in this section is that for a similar antenna dimension, the design of slotted waveguide antennas using CSR slots provides better radiation patterns than the standard rectangular slot arrays while maintaining a similar peak gain.

3. 3D printed HPM antennas

3D printed HPM antennas on ABS

Printing the complementary-split-ring slotted waveguide antenna on ABS plastic was implemented next. The idea of fabricating complex antennas using plastic and then coating them with a conductive material benefits from today's high manufacturing precision and low cost of 3D printing technology and its lightweight. The much reduced dimension of the CSR-SWA compared to the longitudinal slotted waveguide antenna makes the antenna model fits in most commercial 3D printers. Figure 46 shows one of the antennas fabricated using a 3D printer.

The antenna in Figure 47 was printed using a uPRINT SE 3D printer, which can print ABS plus with an accuracy of 100 microns. The total time required to print the complementary-split-ring slotted waveguide antenna was approximately 14 hours.

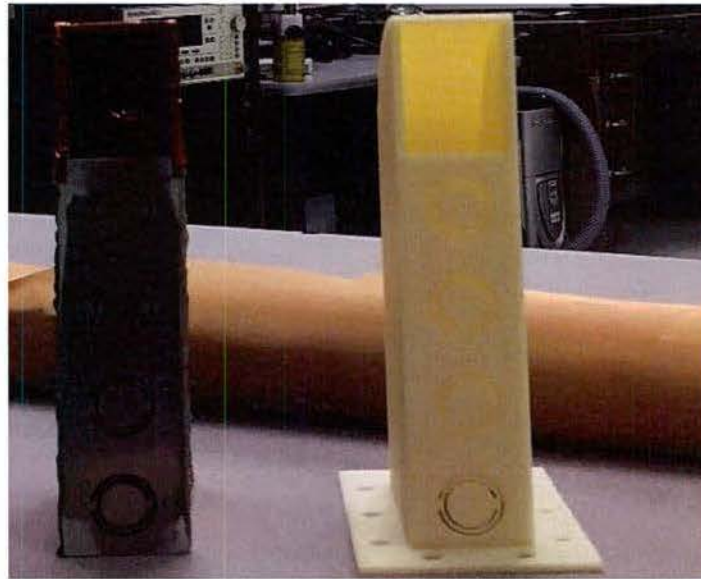


Figure 46. 3D printed CSR-SWA and aluminum CSR-SWA (on the right). Antenna one the left is the metallic version

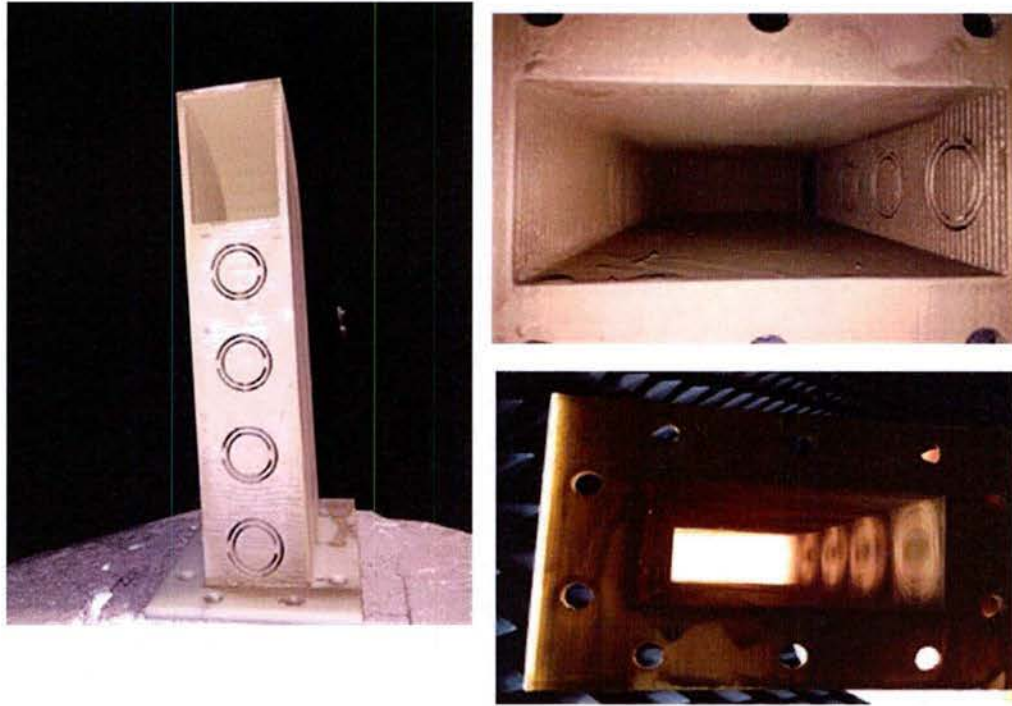


Figure 47. A 3D printed CSR-SWA applied with MG chemical 843 conductive coating

The MG chemical 843 conductive coating was applied to the 3D printed CSR-SWA before testing. The MG chemical 843 is a high conductivity coating designed to reduce electromagnetic or radio frequency interference (EMI/RFI). According to its manufacturer, it provides a low surface resistivity of 0.21 S/square (1.0 mil), which is equal to a bulk conductivity of 1.87×10^5 S/m.

Since the metallic spray is manually applied, control of the metallization thickness uniformity and surface roughness becomes very critical. As expected, a higher surface resistance degrades the gain of the CSR-SWA.

Figure 48 shows the schematic of the antenna that was metallized. An average thickness of 0.3mm of the conductive spray coating was applied to the wall, which is much greater than 0.0065mm, the skin depth of the MG chemical 843 conductive coating at the operating frequency, 3.17GHz. The 3D printed CSR-SWA with conductive coating was modeled in HFSS, as shown in Figure 48.

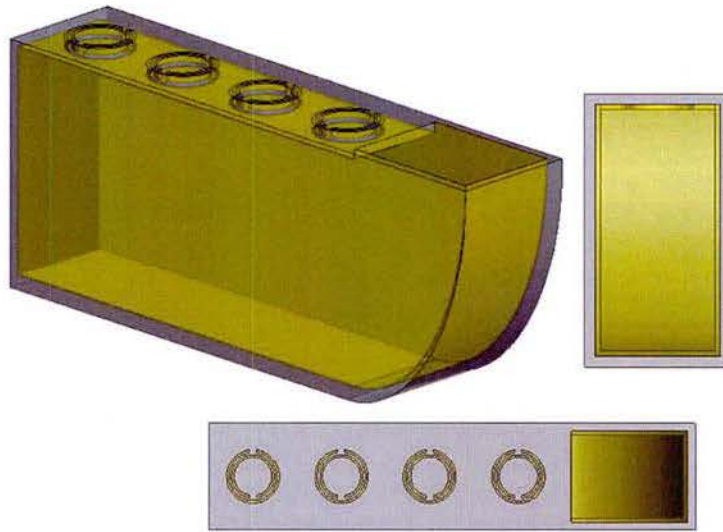


Figure 48. Schematic of 3D printed CSR-SWA with conductive coatings

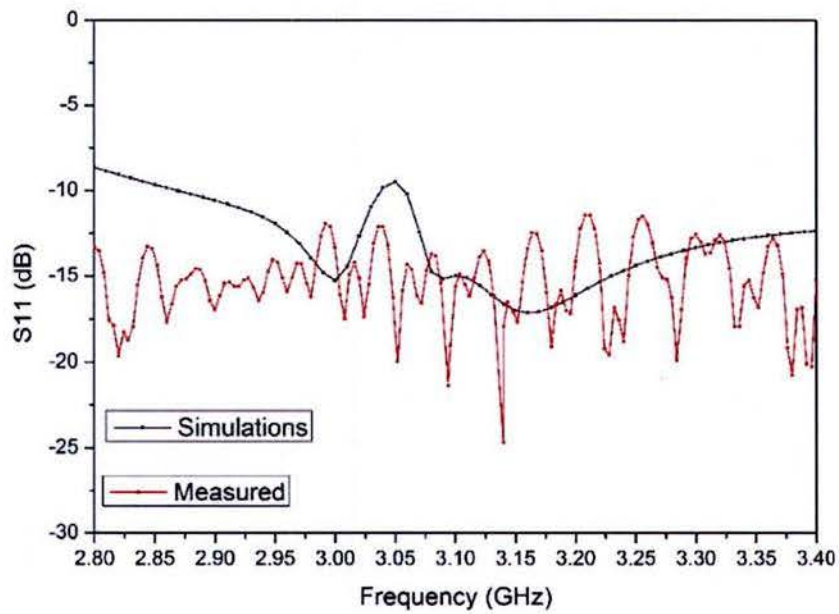


Figure 49. S11 values of 3D printed CSR-SWA with MG chemical 843

A modified model was 3D printed and metallically sprayed. The measured and simulated S11 values are shown in Figure 49. Figures 50 and 51 present the comparison of the radiation patterns of the 3D printed, modified CSR-SWA with conductive coating and the metal CSR-SWA. Despite the manually applied conductive spray, the ABS plastic CSR-SWA coated with metallic paint showed similar radiation

characteristics compared to the metal CSR-SWA.

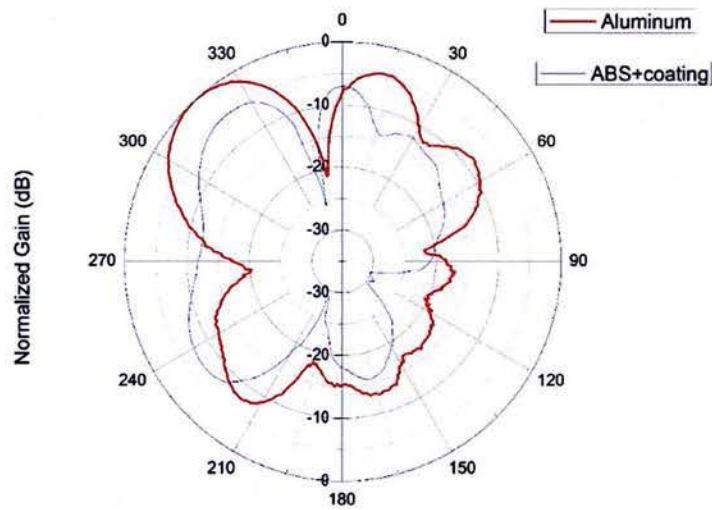


Figure 50. H-plane radiation pattern of 3D printed modified CSR-SWA with conductive coating

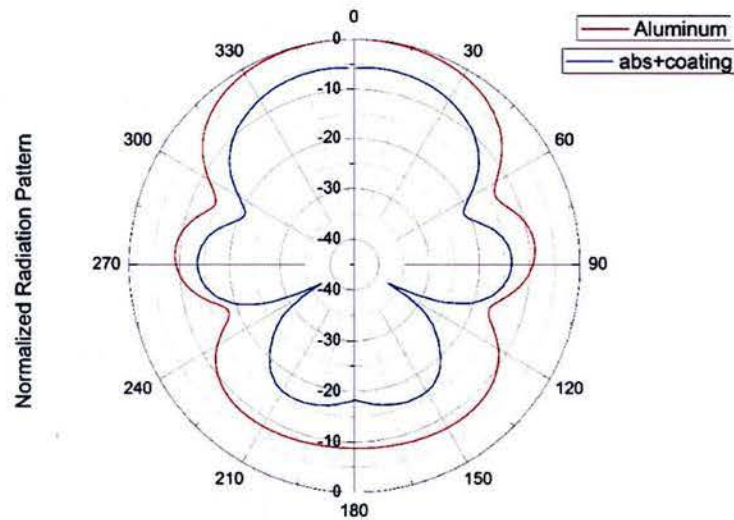


Figure 51. E-plane radiation pattern of 3D printed modified CSR-SWA with conductive coating

Overall, the radiation patterns of the 3D printed array are close to the ones obtained from the equivalent metallic array.

3D printed HPM antennas on Bluestone (SLA printing)

Electroplating was applied next to improve the performance of the 3D printed plastic

antenna. The antenna was plated commercially with a minimum of 5.08 microns of copper everywhere on the surface of the antenna. At 5 GHz, that's 4.37 skin depths of copper, adequate for the metal plated structure to function essentially the same as a solid copper structure. This plating process has significant flexibility to meet RF performance requirements. Meanwhile, the plastic structure is relatively inexpensive, and significantly lighter than a solid metal structure.

Our 3D printed antennas were washed in fresh alcohol and cured with UV light. The ceramic filled stereo lithography (SLA) resin chosen for its stability and stiffness is very opaque to UV light, so it is difficult to post cure the resin with a UV light oven. These resins do thermally cure at elevated temperature or in longer time at room temperature. Parts that are properly cleaned and cured will result in more uniform deposition of nickel and subsequent copper over all surfaces.



Figure 52. SLA printed CSR-SWA plated with copper

The antenna presented in Figure 52 were 3D printed, using SLA 3D printing on a special resin, Bluestone, followed by thorough cleaning and curing performed by

RepliForm Inc.

Usually metal plating thickness is thin enough to be disregarded mechanically i.e. the additional thickness does not affect design parameters enough to be considered. However, in the design of a CSR-SWA, the RF performance of the split-ring slots are sensible to any dimension changes. This antenna has not been tested for high power applications but simulations have shown that it should perform well. This exact value of the power handing capability of 3D printed antennas is a topic of future research endeavors.

IV. CONCLUSIONS

The design of a compact S-band narrow wall complementary-split-ring slotted waveguide antenna loaded with periodic air-filled corrugations was presented and discussed. The antenna is to be approximately vertically front mounted on a land vehicle. The design process of the antenna is a combination of microwave network analysis and full-wave analysis. A set of periodic air-filled corrugations was added to the other narrow-wall of a rectangular waveguide to improve the overall gain. The SWA showed similar radiation characteristics compared to the conventional rectangular slot arrays. The proposed CSR-SWA provided higher peak gain than the conventional $\lambda/4$ rectangular slot array and a more compact size (55% size reduction) compared to the $\lambda/2$ rectangular slot array. Both the theoretic and measured results suggest a return loss less than -30dB which makes the antenna suitable for high power microwave applications.

Further measurements demonstrated the power handling capability of an S-band narrow-wall longitudinal slot antenna. Good agreement between measured and simulated gain was reached. It was shown under high power testing that the peak gain of the antenna was at least 10 dB. Multipactor analysis was applied in the slotted waveguide antenna designs for high-power-microwave applications. Based on experimental and simulation results, it is expected that this narrow-wall slotted waveguide antenna can produce an effective radiated power close to 20 MW.

Finally, a new approach to prototyping CSR-SWA antennas for high-power microwave applications by using 3D printing technology was developed and discussed. 3D printed CSR-SWAs on ABS plastic material yield lightweight antennas with high manufacturing precision compared to standard metallic ones. Measured results show that both the 3D printed and metal CSR-SWA have similar radiation characteristics. Simulation results of the 3D printed antenna suggests good power handling capability.

It shows that 3D printing is capable of providing manufacturing precision for CSR-SWAs that makes fast prototyping of CSR-SWAs for HPM applications possible and cost-effective.

V. List of publications

Journal papers:

- X. Pan, C. G. Christodoulou, "A Narrow-wall Complementary-split-ring Slotted Waveguide Antenna for High-power-microwave Applications," submitted to *IEEE Transactions on Antennas and Propagation*.
- X. Pan, H.S. Faraji, J. McConaha, M. Landavazo, J. Lawrance and C. G. Christodoulou, "Power Handling Capability of a Narrow-wall Slotted Waveguide Antenna," submitted to *IEEE Antennas and Wireless Propagation Letter*.

Conference papers:

- X. Pan, M. Al-Husseini, G. Atmatzakis and C. G. Christodoulou, "A SRR-Loaded sub-wavelength waveguide with H-plane-bend radiator and improved matching for high power application," *2014 United States National Committee of URSI National Radio Science Meeting (USNC-URSI NRSM)*, Boulder, CO, 2014, pp. 1-1.
- X. Pan and C. G. Christodoulou, "A narrow-wall slotted waveguide antenna array for high power applications," *2014 IEEE Antennas and Propagation Society International Symposium (APSURSI)*, Memphis, TN, 2014, pp. 1493-1494.
- X. Pan, M. Al-Husseini, and C. G. Christodoulou, "Miniaturized Slotted Waveguide Antennas with Periodic Structures for HPM Applications", *American Electromagnetics Conference (AMEREM)*, Albuquerque, New Mexico, July 28- Aug 1, 2014.
- X. Pan and C. G. Christodoulou, "A Compact S-band narrow-wall complementary-split-ring slotted waveguide antenna for high power applications," *2015 IEEE International Symposium on Antennas and Propagation & USNC/URSI National Radio Science Meeting*, Vancouver, BC, 2015, pp. 675-676.
- X. Pan, C. G. Christodoulou and J. Lawrance, "Design of high power microwave antennas using 3D printing technology," *2016 IEEE International Symposium on Antennas and Propagation (APSURSI)*, Fajardo, 2016, pp. 821-822.
- X. Pan, J. McConaha, M. Landavazo, J. Lawrance and C. G. Christodoulou, "Cold & Hot Tests of an S-band Antenna for High Power Microwave Systems," *2017 IEEE International Symposium on Antennas and Propagation (APSURSI)*, San Diego, CA, 2017.

APPENDIX I

Slotted circular cylinder resonators

Slotted circular cylinder resonators (SCCRs) are two dimensional analogs of split ring resonators (SRRs), and, for an incident electromagnetic wave with the magnetic field parallel to the cylinder axis, they can provide negative values of magnetic permeability near the magnetic resonance frequency as well. As a result, SCCR structures may serve as an alternative type of metamaterials.

It is known that the artificial magnetism in magnetic resonator structures like SRRs and SCCRs is a local effect due to the internal resonance, instead of arising from the interference between fields radiated by scatterers. As a result, we can focus on the magnetic resonance frequency ω_m of an individual SCCR, instead of that of the periodic SCCR structures.

The resonance behavior of a SCCR is characterized by the radar cross sections (RCSs) with an incident plane wave, whereas the artificial magnetism is identified by its frequency dependence of the magnetic permeability. It is shown that, near the resonance of a SCCR, the frequency dependence of the magnetic polarizability is similar to that in the SRR, corresponding to a magnetic resonance. As a result, the magnetic resonance manifests itself by a peak of the RCS as a function of the incident frequency. So, we can concentrate on the calculation of the RCSs as a function of the incident frequency.

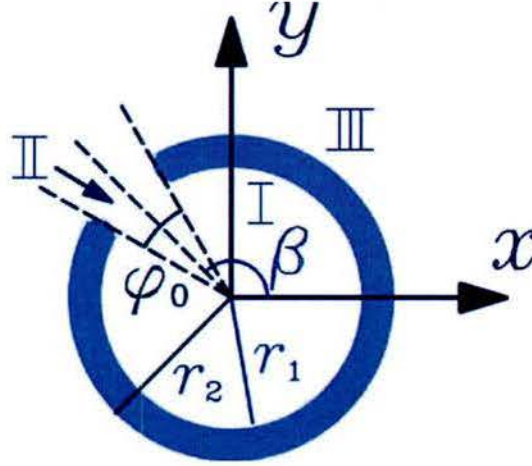


Figure 53. Geometry of SCCR structure with nonzero thickness

The geometry of the SCCR structure is shown in Figure 53. The inner radius of the slotted cylinder shell is r_1 , and the outer radius is r_2 . The extend of the perfect metal of the slotted cylinder is taken between $\varphi_0 < |\varphi - \beta| \leq \pi$. The angular width of the slot is φ_0 and the angle between the center of the slit and x axis is β .

The SCCR structure is illuminated by the TE-polarized plane wave with the magnetic field along the axis of the cylinder. The magnetic field H_z in region I ($r < r_1$), with permittivity ϵ_1 and permeability μ_1 , is expanded as follows:

$$H_z^I = \sum_{m=-\infty}^{\infty} b_m J_m(k_1 r) e^{-im\varphi} \quad (I-1)$$

Where $J_m(x)$ is the Bessel function of order m , $k_1 = k\sqrt{\epsilon_1\mu_1}$ with $k = \omega/c$ the incident wave number.

In region II, we have:

$$H_z^{II} = \sum_{m=0}^{\infty} [D_m J_{v_m}(k_2 r) + E_m Y_{v_m}(k_2 r)] \cos[v_m(\varphi - \tilde{\varphi}_0)] \quad (I-2)$$

Where $Y_h(x)$ is the h th-order Neumann function, $\tilde{\varphi}_0 = \beta - \varphi_0/2$, $v_m = m\pi/\varphi_0$, and $k_2 = k\sqrt{\epsilon_2\mu_2}$ with permittivity ϵ_2 and permeability μ_2 in the slot. Equation I-2

guarantees that E_r vanishes at the wall of the slot. Finally, in the outer space, region III, with permittivity ϵ_0 and permeability μ_0 , H_z is the sum of the incident and scattered fields,

$$H_z^{III} = H_z^{inc} + H_z^{sc} \quad (I-3)$$

$$H_z^{inc} = \sum_{m=-\infty}^{\infty} p_m J_m(kr) e^{-im\varphi} \quad (I-4)$$

$$H_z^{sc} = \sum_{m=-\infty}^{\infty} a_m H_m^{(1)}(kr) e^{im\varphi} \quad (I-5)$$

Where $H_h^{(1)}(x)$ is the h th-order Hankel function of the first kind, p_m and a_m are the expansion coefficients for the incident field and the scattered field, respectively.

Following the method of Serebryannikov and Nosich, from the continuity of H_z and E_φ in the aperture and the vanishing of E_φ inside the metal, the electrical field is cast in the following form:

$$E_\varphi^I(r_1, \varphi) = E_\varphi^{II}(r_1, \varphi) = \sum_{i=1}^M c_i \Theta_i(\varphi) \quad (I-6)$$

$$E_\varphi^{III}(r_2, \varphi) = E_\varphi^{II}(r_2, \varphi) = \sum_{i=1}^M d_i \Theta_i(\varphi) \quad (I-7)$$

Where $\Theta_i(\varphi)$ is the weighted Gegenbauer polynomial of the order -1, which appropriately considers the edge effect. The relation between the scattering coefficients a_m and the incident coefficients p_m in terms of scattering matrix S is:

$$a_m = \sum_{m'} S_{mm'} p_{m'} \quad (I-8)$$

With the scattering matrix S , we can compute the scattering field at any position. The resonance of SCCR is identified by the peak of the normalized RCS as a function of

frequency, with the normalized RCS given

$$\sigma = \frac{1}{\pi r^2} \lim_{r \rightarrow \infty} \frac{2\pi r |H_z^{sc}(r, \varphi_{inc})|^2}{|H_z^{inc}|^2} \quad (I-9)$$

Where φ_{inc} the incident angle of the plane wave.

Near the resonance the frequency dependence of the magnetic polarizability is similar to that in the SRR, corresponding to a magnetic resonance. As a result, the magnetic resonance manifests itself by a peak of the RCS as a function of the incident frequency. To identify the magnetic resonance, we calculate the magnetic polarizability of a single SCCR using the expression:

$$\mathbf{m} = \chi \mathbf{H} \quad (I-10)$$

$$\mathbf{m} = (\mathbf{m}_i + \mathbf{m}_o) / \pi r_2^2 \quad (I-11)$$

$$\mathbf{m}_i = \frac{1}{2} \int \mathbf{r} \times \mathbf{j}_i dS, \quad \mathbf{m}_o = \frac{1}{2} \int \mathbf{r} \times \mathbf{j}_o dS \quad (I-12)$$

where \mathbf{m} is the magnetization density, \mathbf{H} is the magnetic field intensity, and χ is the magnetic polarizability of a SCCR, \mathbf{j}_i (\mathbf{j}_o) is the surface current density on the inner (outer) surface.

Physically, the SRR has been modeled as an L - C circuit system to exhibit its magnetic properties. Similar to SRR structures, the SCCR structure can be modeled as an L - C circuit system, whose capacitance arises from both the cavity of the cylindrical shell and the slot, whereas the inductance comes from the conducting shell.

An approximate expression for the capacitance of the SCCR for small slit width and shell thickness is given by

$$C = \varepsilon_2 \frac{r_2 - r_1}{r_1 \phi_0} + 0.275 \pi \varepsilon_1^{3/4} (r_2 - r_1)^{2/5} (2\pi - \phi_0) \quad (I-13)$$

the inductance of the SCCR is approximated by that of a circular loop, with a small empirical correction taking into account the 2D characteristics and the effect of slit on the cylinder,

$$L = R \left[\ln \left(\frac{8R}{r_2 - r_1} \right) - 2 + \frac{1}{4} \right] \quad (I-14)$$

Thus, the magnetic resonance frequency is evaluated by

$$\omega_m = \frac{1}{\sqrt{LC}} \quad (I-14)$$

The effect of the geometrical parameters of SCCRs on the magnetic resonance have been investigated. Increasing the slit width results in an increase of the magnetic resonance frequency of the SCCR structure. Physically, when the slit width is increased, the capacitance will decrease. In fact, the inductance of the SCCR structure will also decrease when the slit width increases. Decreasing the capacitance and inductance of the system will increase the resonance frequency. However, the change of magnetic resonance with the metal shell thickness is no longer monotonic. Instead, there appears to be an optimal value for the shell thickness that corresponds to the lowest resonance frequency. Only when the shell thickness is larger than this optimal value does increasing the shell thickness result in an increase of the magnetic resonance frequency of the SCCR structure.

REFERENCES

1. J. Benford, J. Swegle, E. Schamiloglu, High Power Microwaves, Boca Raton, FL, USA: CRC Press, 2016.
2. D. V. Giri, "Example scenarios for nonlethal systems," in High-Power Electromagnetic Radiators Nonlethal Weapons and Other Applications. Cambridge, MA: Harvard University Press, 2004, ch. 2, pp. 23-28.
3. W.A. Radasky, C.E. Baum, and M.W. Wik, "Introduction to the special issue on high-power electromagnetics (HPEM) and intentional electromagnetic interference (IEMI)," IEEE Trans. Electromagn. Compat., vol. 46, no. 3, pp. 314-321, Aug. 2004.
4. D.V. Giri and F.M. Tesche, "Classification of intentional electromagnetic environments (IEME)," IEEE Trans. Electromagn. Compat., vol. 46, no.3, pp. 322-328, Aug. 2004.
5. M.R. Lambrecht, K.L. Cartwright, C.E. Baum, and E. Schamiloglu, "Electromagnetic modeling of hot-wire detonators," IEEE Trans. Microw. Theory Tech., vol. 57, no. 7, pp. 1707-1713, Jul. 2009.
6. W. Prather et al., Ultra-wideband source and antenna research, Plasma Science, IEEE Transactions on, vol. 28, no. 5, pp. 1624-1630, 2000.
7. Coburn, W., M. Litz, J. Miletta, N. Tesny, L. Dilks, C. Brown, and B. King, "A slotted-waveguide array for high-power microwave transmission", Army Research Laboratory, January 2001.
8. J. E. Lawrance, C. G. Christodoulou and M. R. Taha, "A High-Power Microwave Zoom Antenna With Metal-Plate Lenses," in IEEE Transactions on Antennas and Propagation, vol. 63, no. 8, pp. 3380-3389, Aug. 2015.
9. J. Zhao, H. Li and T. Li, "Design of a double square rings element for high-power X-band reflectarray antenna," 2015 IEEE International Vacuum Electronics Conference (IVEC), Beijing, 2015, pp. 1-2.
10. X.-Q. Li, Q.-X. Liu, X.-J. Wu, L. Zhao, J.-Q. Zhang, and Z.-Q. Zhang, "A GW level high-power radial line helical array antenna", IEEE Trans. Antennas Propag., vol. 56, no. 9, pp. 2943-2948, Sep. 2008.
11. K.J. Nicholson, W.S.T. Rowe, P.J. Callus, and K. Ghorbani, "Split-ring resonator loading for the slotted waveguide antenna stiffened structure," IEEE Antennas Wireless Propag. Lett., vol. 10, pp. 1524-1527, 2011.
12. K.J. Nicholson, W.S.T. Rowe, P.J. Callus, and K. Ghorbani, "Small slot design for slotted waveguide antenna stiffened structure," Electron. Lett., vol. 48, pp. 676-677, 2012.
13. A. Daliri, W. S. T. Rowe and K. Ghorbani, "Slotted waveguide antenna array using complimentary split ring resonator elements," 2014 International Workshop on Antenna Technology: Small Antennas, Novel EM Structures and Materials, and Applications (iWAT), Sydney, NSW, 2014, pp. 344-347.
14. A. Daliri, W.S.T. Rowe, K. Ghorbani, "Split-Ring Slot in the Broad-Wall of a

- Rectangular Waveguide”, *Antennas and Wireless Propagation Letters*, IEEE, vol.13, pp.991-994, 2014.
15. J. Czyzewska, P. Burzynska, K. Gawelb, and J. Meisnerc, “Rapid prototyping of electrically conductive components using 3D printing technology,” *J. Mater. Process. Technol.*, vol. 209, no. 12–13, pp. 5281–5285, Jul. 1, 2009, ISSN 0924-0136/10.1016/j.jmatprotec. 2009.03.015.
 16. N. M. Jordan, G. B. Greening, S. C. Exelby, R. M. Gilgenbach, Y. Y. Lau and B. W. Hoff, "Additively manufactured anodes in a relativistic Planar Magnetron," 2016 IEEE International Vacuum Electronics Conference (IVEC), Monterey, CA, 2016, pp. 1-2.
 17. D. M. French, D. Shiffler, "High power microwave source with a three dimensional printed metamaterial slow-wave structure", *Appl. Phys. Lett.*, vol. 87, no. 5, pp. 053308, May 2016.
 18. X. Pan, “S band narrow-wall slotted waveguide antenna for high-power applications”. Master thesis, University of New Mexico, Albuquerque, New Mexico, December 2012.
 19. D. R. Lide, Ed., Table 1. Dielectric strength of gases, in *CRC Handbook of Chemistry and Physics*, (Internet Version 2009), 89th ed., CRC Press/Taylor & Francis, Boca Raton, FL.
 20. J. A. Rees, editor; Figure 3. Calculated (x) and observed (o) sparking potentials in air in *Electrical Breakdown in Gases*, Halsted Press/John Wiley & Sons, New York, 1973.
 21. J. R. M. Vaughan, “Multipactor, in *IEEE Transactions on Electron Devices*, vol. 35, no. 7, pp. 1172-1180, Jul 1988.
 22. S. Riyopoulos, Multipactor saturation due to space-charge-induced debunching, *Phys. Plasmas*, vol. 4, no. 5, pp. 1448-1462, 1997.
 23. E. Sorolla, A. Sounas, and M. Mattes, Space charge effects for multipactor in coaxial lines, *Phys. Plasmas*, vol. 22, no. 3, p. 033512, 2015.
 24. M. A. Furman and M. T. F. Pivi, “Probabilistic model for the simulation of secondary electron emission,” *Phys. Rev. Special Topics Accel. Beams*, vol. 5, no. 1, pp. 124404-1-124404-18, 2002.
 25. J. R. M. Vaughan, “A new formula for secondary emission yield,” in *IEEE Transactions on Electron Devices*, vol. 36, no. 9, pp. 1963-1967, Sep 1989.